
COMPARATIVE ANALYSIS OF METHODS FOR CLOUD SEGMENTATION IN INFRARED IMAGES

Guillermo Terrén-Serrano

Department of Electrical and Computer Engineering
The University of New Mexico
Albuquerque, NM 87131, United States
guillermoterren@unm.edu

Manel Martínez-Ramón

Department of Electrical and Computer Engineering
The University of New Mexico
Albuquerque, NM 87131, United States
manel@unm.edu

May 29, 2022

ABSTRACT

The increasing penetration of Photovoltaic (PV) systems in the power network makes the grid vulnerable to the projection of cloud shadows over PV systems. Real-time segmentation of clouds in infrared (IR) images is important to reduce the impact of noise in the short-term forecast of Global Solar Irradiance (GSI). This investigation presents a comparison between discriminate and generative models for cloud segmentation. Markov Random Fields (MRF), which add information from neighboring pixels to the prior, are included among the analyzed generative models. This investigation includes an evaluation of the performance of supervised and unsupervised learning methods in cloud segmentation. The discriminate models are solved in the primal formulation to make them feasible in real-time applications. The performances are compared using the j-statistic. Preprocessing of IR images to remove stationary artifacts increases the overall performances in all of the analyzed methods. The inclusion of features from neighboring pixels in the feature vectors leads to an improvement in the performances in some of the cases. The MRFs achieve the best performance in both unsupervised and supervised generative models. The discriminate models solved in the primal yield a dramatically lower computing time along with high performance in the segmentation. The performances of the generative models are comparable to those of the discriminate models when proper preprocessing is applied to the IR images.

Keywords Cloud Segmentation · Machine Learning · Markov Random Field · Sky Imaging · Solar Forecasting

1 Introduction

A large power grid system fully operated using only renewable power is a feasible scenario by 2050 [1]. Clouds increase or decrease the solar irradiance that reaches the Earth's surface [2]. This is of great importance when a considerable percentage of the energy in a power grid is generated using large PV systems [3]. Even when the PV arrays in a power plant are arranged in a configuration capable of attenuating the effects caused by moving clouds, the projection of cloud shadows produce interruptions in energy generation which may be out of the grid operator's admissible range [4]. The effects of clouds on solar irradiance also appears in other energy generation systems using solar energy as resource [5]. When cloud information is included in forecasting of solar irradiance the overall performance is improved [6].

Computer recognition of clouds is a geospatial information problem [7]. The Tropopause limits the range of clouds formations, which seasonally varies across latitudes [8]. Different cloud types are expected to be found at a different range of altitudes [9]. When using features extracted from color intensity channels, cloud patterns inferred from data acquiesced at different latitudes may not be correlated. Methods that use features extracted based on texture analysis with Gabor filters and statistics are more easily replicable across databases [10].

In GSI forecasting, the horizons of ground-based methods (without features extracted from clouds) are in the range of hours [11, 12, 13, 14, 15, 16]. Accuracy can be improved using satellite images [17] to asses the effects of clouds on

ground-level solar irradiance [18, 19]. Cloud forecasting allows us to control home appliances in events when the Sun is occluded [20, 21, 22]. Ground measurements are not capable of predicting when a cloud will abruptly affect a PV system [23]. The usage of ground-based sky imaging is the most suitable method in applications which require very short-term GSI forecasting [24].

When using visible light sensors, the circumsolar region appears saturated in images with the Sun in the frame [25, 26, 27, 28]. Built-in structures to block the Sun’s direct radiations partially obstruct the images [29, 30, 31, 32], creating a problem in forecasting GSI [33]. Nevertheless, Total Sky Imagery (TSI) [29, 34, 35], and fisheye lenses are capable of recording large Field of View (FOV) [26]. When any of these technologies is applied with the aim of motion estimation, the fisheye lens’ distortion should be removed [25]. Velocity vectors are computed in pixels per frame, and fisheye distortions cause the dimensions of pixels to vary across spatial areas. With recent improvements in IR imaging, large FOV thermal images are also possible [36]. IR images allow the derivation of physical features of the clouds such as temperature [37] and height, which are more interpretable for modelling physical processes. In fact, ground-based IR cameras providing radiometric measures [38, 39], were used to study statistical features of clouds [40], and in applications involving earth-space communications [41]. Further research shows how to stabilize the thermal image from microbolometers when doing atmospheric measurements [42].

Previous investigations in cloud segmentation concluded that the segmentation of a pixel using features extracted from neighboring pixels yields an improvement in performance [25, 43, 44]. Graph models based on neighboring pixels’ classification are referred to as MRFs. These models are a generalization of the Ising Model, which was first introduced in the context of ferromagnetic problems [45], and was later applied to 2-dimensional crystal lattice problems [46]. The Iterated Conditional Modes (ICM) algorithm was developed for unsupervised training of MRF in image processing [47], and was implemented for cloud segmentation using IR satellite images [48], and visible light ground-based images [49].

The superpixel approach speeds-up computing time, however it produces a coarse segmentation [10, 30, 32, 44, 50]. Real-time cloud segmentation is a problem for kernel learning methods, as the Gram matrix is generally dense [28, 51]. One alternative is the use of regularized non-linear methods formulated in the primal. The same problem appears when Convolutional Neural Networks (CNN) are trained for segmenting images. The computing time required is high [10, 27], although it is considerably reduced when hardware acceleration is implemented using GPUs in parallel [52, 53]. Nevertheless, these methods require data augmentation and regularization techniques to avoid overfitting. Otherwise, the conclusions obtained are not comparable between different clouds’ databases, since the distribution of the features will vary.

Kernel methods and CNNs have high computational cost, which makes real-time segmentation difficult. We prove that when effective preprocessing is applied to the IR images to extract informative physical features, discriminate models are faster and have similar accuracy to generative, kernel or deep learning methods

This research contributes to the field through the analysis of data acquiesced from a ground-based radiometric long-wave IR imagery system. This system, which is mounted on a solar tracker, supplies thermal images that allow the extraction of physical features of clouds for segmentation. Debris such as water stains and dust may appear on outdoor Data Acquisition (DAQ) systems exposed to weather. The preprocessing algorithm applies two models to the IR images. With the first model, debris is removed from the IR images implementing a persistent model of the camera’s window [54]. With the second, the direct radiation from the Sun and the scatter radiation from the atmosphere are modelled as cycle-stationary and removed from the IR images. To our knowledge, no literature that deals with this problem related to ground-based cloud image acquisition has been published.

We implement discriminative methods solved in the primal for cloud segmentation, Ridge Regression (RR), Support Vector Classifier (SVC) and Gaussian Process (GP). We compare them with supervised generative methods: MRF and Naive Bayes Classifier (NBC); as well as unsupervised methods: Gaussian Mixture Model (GMM) and k-means clustering. This comparative analysis includes methods that are in the literature such as Gaussian Discriminate Analysis (GDA) and ICM-MRF. The implementation of a voting scheme among different methods has been shown to improve the overall segmentation performances [43]. We find that the combination of the models that yields an improvement in the segmentation performances.

2 Feature Extraction

The features from the IR images are extracted after applying a processing to remove the Sun, and Atmosphere scattering effects. The IR camera’s window cannot be routinely cleaned because of difficult access to the DAQ localization. Therefore, we propose a persistent model to remove the effects produced by the dust particles and water spots on the window that uses weather measures from a nearby weather station [54]. The features extracted from the IR images

and the pixel's neighborhood configuration are cross-validated in order to find the set of features that increases the segmentation performances in each method.

2.1 Infrared Images

A pixel of the camera frame is defined by a pair of Euclidean coordinates i, j . The temperature of a particle in the Troposphere is a function of the height, so that the height of a pixel in a frame can be approximated using the Moist Adiabatic Lapse Rate (MALR) function [55, 56], that we define as $\phi : T \mapsto H$. The cloud temperature image $\mathbf{T} = \{T_{i,j} \in \mathbb{R}^+ \mid \forall i = 1, \dots, M, \forall j = 1, \dots, N\}$ in Kelvin degrees, is measured with an IR camera. The heights of the pixels are defined in kilometers as $\mathbf{H} = \{H_{i,j} \in \mathbb{R}^+ \mid \forall i = 1, \dots, M, \forall j = 1, \dots, N\}$ and they are computed using the MALR function.

A multi-class classification model determines the sky conditions in an IR image. The classes of sky conditions are: clear, cumulus, stratus or nimbus. The model uses the temperature of the pixels, the magnitude of the velocity vectors, the atmospheric pressure and the clear-sky index to perform a classification [54]. When the sky conditions are detected as clear, the IR image is added to the clear-sky set. At the same time, the algorithm forgets the oldest clear-sky image in the set. The set is defined as the last $L = 250$ clear-sky IR images. The sky-condition of an IR image is the persistent class obtained in the last $\ell = 3$ classifications. The scatter radiation produced by dust and water stains on the window's lens is the median image computed using the IR images in the clear-sky set. The obtained temperature of each pixel, after removing the dust and stains, is defined as $\mathbf{T}' = \{T'_{i,j} \in \mathbb{R}^+ \mid \forall i = 1, \dots, M, \forall j = 1, \dots, N\}$, and the heights are $\mathbf{H}' = \{H'_{i,j} \in \mathbb{R}^+ \mid \forall i = 1, \dots, M, \forall j = 1, \dots, N\}$.

Deterministic components of the GSI are modelled and removed from the IR images. The raw intensity of a pixel is processed to remove the direct radiation from the Sun, and the scatter radiation from the atmosphere. The parameters of the scatter radiation model are variables that depend on the day, air temperature, dew point, elevation and azimuth. The parameters of Sun's direct radiation model are constants. After removing both the window model and the atmospheric model from the images, difference of temperatures with respect to the Tropopause's temperature are defined as $\Delta\mathbf{T} = \{\Delta T_{i,j} \in \mathbb{R} \mid \forall i = 1, \dots, M, \forall j = 1, \dots, N\}$. The difference of heights are also computed and multiplied by the Tropopause's average temperature in the image, estimated using the atmospheric background model. The resulting heights are $\mathbf{H}'' = \{H''_{i,j} \in \mathbb{R}^+ \mid \forall i = 1, \dots, M, \forall j = 1, \dots, N\}$.

The temperature differences are normalized to 8 bits, $\mathbf{I} = \{i_{i,j} \in \mathbb{N}^{2^8} \mid \forall i = 1, \dots, M, \forall j = 1, \dots, N\}$. The lowest value is set to 0, and then divided by the clouds' maximum feasible temperature. The feasible temperature is calculated assuming a linear temperature decrease of $9.8^\circ\text{K}/\text{km}$ in the Tropopause [57], and that the average Tropopause height is 11.5km at 36° latitude north [58]. The average height above sea level is 1.52km in Albuquerque, NM.

The velocity vectors were computed applying the Weighted Lucas-Kanade method (WLK) [22, 59]. For each two consecutive images $\mathbf{I}^{k-1}, \mathbf{I}^k$ of the data set, the velocity vectors are defined as $\mathbf{V}^k = \{\mathbf{v}_{i,j} = (u, v)_{i,j}^k \in \mathbb{R}^2 \mid \forall i = 1, \dots, M, \forall j = 1, \dots, N\}$. The upper index k denoting the frame is omitted in the rest of the document.

2.2 Feature Vectors

In order to find the optimal feature combination, we propose to validate different physical features extracted from a pixel, and three structures of neighboring pixels to include as dependent variable in the model.

The first feature vector, $\mathbf{x}_{i,j}^1 = \{T_{i,j}, H_{i,j}\}$, contains the raw radiometric temperature of the pixels and the heights computed using the raw temperatures. The second feature vector, $\mathbf{x}_{i,j}^2 = \{T'_{i,j}, H'_{i,j}\}$, contains the temperature and height of the pixels after removing the artifacts on the IR camera's window. The third feature vector, $\mathbf{x}_{i,j}^3 = \{\Delta T_{i,j}, H''_{i,j}\}$, contains the incremental temperatures and heights after removing the Sun's direct radiation and the atmosphere's scatter radiation and the heights. The fourth feature vector includes the magnitude of the velocity vectors, the normalized intensities, and the increments of temperature, and it is defined as $\mathbf{x}_{i,j}^4 = \{\text{mag}(\mathbf{v}_{i,j}), i_{i,j}, \Delta T_{i,j}\}$.

In order to segment a pixel, its feature vectors and those of its neighbour pixels are introduced in the classifier. In the experiments, we define *1st order neighborhood* feature vector as the set of four pixels closest to pixel under test i, j , *2nd order neighborhood* is defined as the eight closest pixels, and term *single pixel* is used when no neighbors are included, this is:

- Single pixel: $\{\mathbf{x}_{i,j}\}, \quad \forall i, j = i_1, j_1, \dots, i_M, j_N$
- 1st order neighborhood: $\{\mathbf{x}_{i-1,j}, \mathbf{x}_{i,j-1}, \mathbf{x}_{i,j+1}, \mathbf{x}_{i+1,j}\}.$
- 2nd order neighborhood: $\{\mathbf{x}_{i-1,j}, \mathbf{x}_{i,j-1}, \mathbf{x}_{i,j+1}, \mathbf{x}_{i+1,j}, \mathbf{x}_{i-1,j-1}, \mathbf{x}_{i-1,j+1}, \mathbf{x}_{i+1,j-1}, \mathbf{x}_{i+1,j+1}\}.$

3 Methods

Fine cloud image segmentation performed in real-time without applying down-sampling techniques, requires approaches that are computationally light. In general, we require methods whose image segmentation time is much shorter than the image acquisition rate. For example, in the present application, the image acquisition period is of the order of 10s, so we require a segmentation time of less than 1 second. Deep learning is computationally expensive for this application when single CPU computers are used and therefore, it is not considered for this study. Similarly, kernel machines may be computationally expensive since their test time is proportional to the number of training data, so they cannot be used in the original dual formulation. When the Hilbert space in which the machine is formulated has finite dimension, an alternative primal formulation can be used with a test time proportional to the Hilbert space dimension. This is the strategy followed in this work. Sparse kernel methods can also be applied [60] but they have not been considered in this research.

The methods described below can be classified as generative when they have the capacity of generating new samples from a likelihood model, this is, when the model implements a density approximation of the form $p(\mathbf{x}|\mathcal{C}_k)$ where \mathcal{C}_k is the segmentation label of the pixel. Discriminative models do not have the ability to generate data since they implement a direct approximation of the posterior $p(\mathcal{C}_k|\mathbf{x})$.

3.1 Generative Models

From the point of view of the level of inference applied, the generative models summarized here can be classified either as Maximum Likelihood (ML) methods, or Maximum a Posteriori (MAP) methods. Besides, when generative models use an input feature structure, together with the use of an energy function for the probabilistic modeling of the data (Ising model), they are generally known as MRF models. Among all generative models, we summarize below the discriminant analysis, which apply ML inference, GMM and k-means clustering, and supervised and unsupervised MRF methods. These methods use MAP inference.

3.1.1 Discriminant Analysis

GDA and NBC are both supervised learning methods, because the training dataset input features \mathbf{x}_i are paired with a label \mathcal{C}_k . As we assume that the prior in this models is uniform, the inference applied is ML.

Gaussian Discriminant Analysis. GDA obtains the posterior probability of $y_i = \mathcal{C}_k$ given a set of features $\mathbf{x}_i \in \mathbb{R}^d$ applying the Bayes theorem [61],

$$p(\mathcal{C}_k | \mathbf{x}_i) = \frac{p(\mathcal{C}_k) p(\mathbf{x}_i | \mathcal{C}_k)}{p(\mathbf{x}_i)} \propto p(\mathcal{C}_k) \cdot p(\mathbf{x}_i | \mathcal{C}_k) \quad (1)$$

where $p(\mathbf{x}_i)$ is a marginal likelihood over a \mathbf{x}_i , a Multinoulli mass function $p(\mathcal{C}_k)$ is the prior probability of a class \mathcal{C}_k , and $k \in \{1, \dots, K\}$ are possible classes.

We assume that the likelihood is a multivariate normal distribution,

$$p(\mathbf{x}_i | \mathcal{C}_k) = \frac{1}{\sqrt{(2\pi)^d |\Sigma_k|}} \cdot \exp \left\{ -\frac{1}{2} (\mathbf{x}_i - \boldsymbol{\mu}_k)^\top \Sigma_k^{-1} (\mathbf{x}_i - \boldsymbol{\mu}_k) \right\}, \quad (2)$$

where $\boldsymbol{\mu}_k \in \mathbb{R}^d$ and $\Sigma_k \in \mathbb{R}^{d \times d}$ are the sample mean and covariance function computed using only the samples that have assigned class \mathcal{C}_k and d is the sample dimension, i.e, the number of features in vector \mathbf{x}_i .

The classification for a sample follows the MAP criterion,

$$\hat{y}_i = \underset{k}{\operatorname{argmax}} p(\mathcal{C}_k) \cdot p(\mathbf{x}_i | \mathcal{C}_k). \quad (3)$$

as we assume that the $p(\mathcal{C}_k) = 1/K$ is uniform, this is equivalent to a ML classifier,

$$\hat{y}_i = \underset{k}{\operatorname{argmax}} p(\mathbf{x}_i | \mathcal{C}_k). \quad (4)$$

Statistics $\boldsymbol{\mu}_k$ and Σ_k are the sample mean and covariance approximated by using a set of labelled training data.

Naive Bayes Classifier. The NBC applies the Bayes theorem, similarly to a ML classifier, but it computes a likelihood by assuming that all features are independent. It is equivalent to a GDA where the covariance matrix of the likelihood is a diagonal matrix [62],

$$p(\mathcal{C}_k | \mathbf{x}) = \frac{p(\mathcal{C}_k) p(\mathbf{x} | \mathcal{C}_k)}{p(\mathbf{x})} \propto p(\mathcal{C}_k, x_1, \dots, x_d) \quad (5)$$

where x_j are the features of each sample vector \mathbf{x} .

Applying the naive conditional independent assumption between the features for simplification, is obtained that,

$$p(x_j | x_{j+1}, \dots, x_d, \mathcal{C}_k) = p(x_j | \mathcal{C}_k). \quad (6)$$

At this point, when the chain rule is applied, the model can be expressed as product of factorized probabilities,

$$\begin{aligned} p(\mathcal{C}_k | x_1, \dots, x_d) &\propto p(\mathcal{C}_k, x_1, \dots, x_d) \\ &= p(\mathcal{C}_k) p(x_1 | \mathcal{C}_k) p(x_2 | \mathcal{C}_k) p(x_3 | \mathcal{C}_k) \dots \\ &= p(\mathcal{C}_k) \prod_{j=1}^d p(x_j | \mathcal{C}_k). \end{aligned} \quad (7)$$

A class is assigned to a sample \mathbf{x}_i applying ML classification criteria that is defined as,

$$\hat{y}_i = \operatorname{argmax}_k \prod_{j=1}^d p(x_{i,j} | \mathcal{C}_k), \quad (8)$$

which is equivalent to maximizing the posterior (7) since the prior of a class $p(\mathcal{C}_k)$ is assumed to be uniform, in the same way that GDA.

The naive classifier in our application is implemented using a normal distribution for each feature x_j in a class \mathcal{C}_k ,

$$p(x_j | \mathcal{C}_{j,k}) = \frac{1}{\sqrt{2\pi\sigma_{j,k}^2}} \exp \left\{ -\frac{(x_j - \mu_{j,k})^2}{2\sigma_{j,k}^2} \right\}, \quad (9)$$

where $\mu_{j,k}$ and $\sigma_{j,k}$ are the sample mean and variance for the feature x_j in class \mathcal{C}_k .

3.1.2 Clustering

GMM and the k-means are unsupervised learning algorithms. Their respective objective functions group the samples in clusters represented by conditional likelihood functions, and then a posterior distribution for each class \mathcal{C}_k is computed with the likelihood and a prior distribution of the labels. Thereby, the inference level applied is MAP. k-means can be considered as a simplification of the GMM.

Gaussian Mixture Model. The distribution of the features can be approximate by a mixture of multivariate normal distributions $\mathbf{x}_i \sim \mathcal{N}(\boldsymbol{\mu}_k, \boldsymbol{\Sigma}_k)$. Under the hypothesis that a sample \mathbf{x}_i belongs to class \mathcal{C}_k , its class conditional likelihood is

$$f(\mathbf{x}; \boldsymbol{\mu}_k, \boldsymbol{\Sigma}_k) = \frac{1}{\sqrt{(2\pi)^d |\boldsymbol{\Sigma}_k|}} \cdot \exp \left\{ -\frac{1}{2} (\mathbf{x} - \boldsymbol{\mu}_k)^\top \boldsymbol{\Sigma}_k^{-1} (\mathbf{x} - \boldsymbol{\mu}_k) \right\}. \quad (10)$$

The log-likelihood of the multivariate density function [62], that we need for computing the expected complete data log-likelihood in the GMM is,

$$\log p(\mathbf{x}_i | \boldsymbol{\mu}_k, \boldsymbol{\Sigma}_k) = -\frac{d}{2} \log 2\pi - \frac{1}{2} \log |\boldsymbol{\Sigma}_k| - \frac{1}{2} (\mathbf{x}_i - \boldsymbol{\mu}_k)^\top \boldsymbol{\Sigma}_k^{-1} (\mathbf{x}_i - \boldsymbol{\mu}_k). \quad (11)$$

The expected complete data log-likelihood is,

$$\mathcal{Q}(\boldsymbol{\theta}^{(t)}, \boldsymbol{\theta}^{(t-1)}) = \sum_{i=1}^N \sum_{k=1}^K \gamma_{i,k} \log \pi_k + \sum_{i=1}^N \sum_{k=1}^K \gamma_{i,k} \log p(\mathbf{x}_i | \boldsymbol{\theta}^{(t)}) \quad (12)$$

where $\gamma_{i,k} \triangleq p(y_i = k | \mathbf{x}_i, \boldsymbol{\theta}^{(t-1)})$ is the responsibility of the cluster k in the sample i .

The parameters in the clustering of multivariate normal distributions can be directly computed applying the Expectation Maximization (EM) algorithm. In the E stage of the algorithm a prior is established and then, by using the likelihood function (10), a posterior $\gamma_{i,k} = p(\mathcal{C}_k | \mathbf{x}_i)$ can be assigned to each sample. In the M stage, the mean and variance of each cluster that maximize the log likelihood are computed as

$$\boldsymbol{\mu}_k = \frac{\sum_{i=1}^N \gamma_{i,k} \cdot \mathbf{x}_i}{\gamma_k}, \quad \boldsymbol{\Sigma}_k = \frac{\sum_{i=1}^N \gamma_{i,k} \cdot \mathbf{x}_i \mathbf{x}_i^\top}{\gamma_k} - \boldsymbol{\mu}_k \boldsymbol{\mu}_k^\top. \quad (13)$$

The priors are updated as well using the posterior probabilities that are

$$\pi_k = p(C_k) = \frac{1}{N} \sum_{i=1}^N \gamma_{i,k}, \quad (14)$$

where N is the number of available samples. A class is assigned to each sample by MAP criteria,

$$\hat{y}_i = \underset{k}{\operatorname{argmax}} p(C_k | \mathbf{x}_i, \boldsymbol{\mu}_k, \boldsymbol{\Sigma}_k) \quad (15)$$

The theory behind mixture models, as well as the EM algorithm, is fully developed in [62].

k-means. This clustering algorithm is a particular case of a GMM, in which the covariance matrices $\boldsymbol{\Sigma}_k = \mathbf{I}_{d \times d}$, and the responsibilities $\pi_k = 1/K$ are assumed constants [63, 62]. The posterior distribution is discretized, this is, $p(y_i = k | \boldsymbol{\mu}_k, \boldsymbol{\Sigma}_k) \approx \mathbb{I}(k = y_i)$, and since each clusters has the same spherical variance, the nearest cluster center is,

$$\hat{y}_i = \underset{k}{\operatorname{argmin}} \|\mathbf{x}_i - \boldsymbol{\mu}_k\|_2^2. \quad (16)$$

The k-means attends to minimize the distance between each sample \mathbf{x}_i to a class center $\boldsymbol{\mu}_k$. The criteria of assignment a sample to a cluster center is based on minimum squared Euclidean distance of a sample i to each cluster center k , and it is computed at each step t as an iterative optimization method. First, for each cluster, a set $S_k^{(t)}$ is defined as the set of data whose closer cluster is defined by mean $\boldsymbol{\mu}_k$, i. e.:

$$S_k^{(t)} = \left\{ \mathbf{x}_i : \|\mathbf{x}_i - \boldsymbol{\mu}_k^{(t)}\|_2^2 \leq \|\mathbf{x}_i - \boldsymbol{\mu}_{-k}^{(t)}\|_2^2, \forall k = 1, \dots, K \right\}. \quad (17)$$

This is indeed the fundamental difference with a GMM from the geometric point of view, since the GMM is based on the minimization of Mahalanobis distance.

After assigning each sample to a cluster, the cluster centers are computed applying the sample mean formula, but only using the samples that belong to each one of the clusters.

$$\boldsymbol{\mu}_k^{(t+1)} = \frac{1}{|S_k^{(t)}|} \sum_{\mathbf{x}_i \in S_k^{(t)}} \mathbf{x}_i, \quad (18)$$

where $|\cdot|$ is the cardinality of the sample set from cluster k .

The measure of the distance between a sample and the centred of its cluster, is transformed into a probability,

$$p(C_k | \mathbf{x}_i) = 1 - \frac{\|\mathbf{x}_i - \boldsymbol{\mu}_k\|^2}{\sum_{k=1}^K \|\mathbf{x}_i - \boldsymbol{\mu}_k\|^2}, \quad (19)$$

so that the MAP criterion can be applied afterwards.

3.1.3 Markov Random Fields

The energy function of a MRF is composed of two functions [64]. The function φ that is the joint distribution of a class, and the function ψ that is the potential energy of the system's configuration (a term from statistical mechanics),

$$\mathcal{E}(y_i, \mathbf{x}_i) = \sum_i \varphi(\mathbf{x}_i, y_i) + \sum_{i,j} \psi(y_i, y_j), \quad (20)$$

where \mathbf{x}_i is the feature vector of sample i and y_i is its class. In the graph G , a sample i has a set of neighboring pixels, and each neighboring sample j has class y_j .

A probabilistic perspective is implemented to infer the optimal set of parameters $\boldsymbol{\theta}_k$ of the energy function. A sample \mathbf{x}_i is classified using the Bayes' theorem,

$$\begin{aligned} p(y_i = C_k | \mathbf{x}_i, \boldsymbol{\theta}_k) &= \frac{p(\mathbf{x}_i | y_i = C_k, \boldsymbol{\theta}_k) \cdot p(y_i = C_k)}{p(\mathbf{x}_i)} \\ &\propto p(\mathbf{x}_i | y_i = C_k, \boldsymbol{\theta}_k) p(y_i = C_k). \end{aligned} \quad (21)$$

In the problem of cloud segmentation, the likelihood of the feature vectors is approximated by a multivariate normal distribution $\mathbf{x}_i \sim \mathcal{N}(\boldsymbol{\mu}_k, \boldsymbol{\Sigma}_k)$ of class \mathcal{C}_k ,

$$p(\mathbf{x}_i | y_i = \mathcal{C}_k, \boldsymbol{\theta}_k) = \frac{1}{\sqrt{(2\pi)^d |\boldsymbol{\Sigma}_k|}} \exp \left\{ -\frac{1}{2} (\mathbf{x}_i - \boldsymbol{\mu}_k)^\top \boldsymbol{\Sigma}_k^{-1} (\mathbf{x}_i - \boldsymbol{\mu}_k) \right\}, \quad (22)$$

where $\boldsymbol{\theta}_k = \{\boldsymbol{\mu}_k, \boldsymbol{\Sigma}_k\}$ are the parameters set of the feature distribution in class \mathcal{C}_k , and d is the number of features in vector $\mathbf{x}_i \in \mathbb{R}^d$. The log-likelihood of class \mathcal{C}_k is defined as $\varphi(\mathbf{x}_i, y_i) \triangleq \log p(\mathbf{x}_i | y_i = \mathcal{C}_k, \boldsymbol{\theta}_k)$ in the energy function (20). The prior can be expressed as,

$$p(y_i) = \frac{1}{Z} \exp(-\psi(y_i)) = \frac{1}{Z} \exp \left(- \sum_{\Omega_\ell \in \Omega} V_{\Omega_\ell}(y_i) \right). \quad (23)$$

By applying the Hammersley–Clifford theorem [65], the potential function $\psi(y_i)$ in the exponential form can be factorized in cliques of a graph G . A clique is defined as a set of nodes that are all neighbors of each other [62]. In this way, the potential function can be independently evaluated for each clique in the factorized graph,

$$\psi(y_i) = \sum_{\ell=1}^L \left(\sum_{i,j \in \Omega_\ell} y_i \beta y_j \right), \quad (24)$$

where the set of maximal cliques in the graph is defined as $\Omega = \Omega_1 \cup \Omega_2 \cup \dots \cup \Omega_L$, ℓ represents the order of the neighboring pixels to sample i in the graph network G , and Ω_L is the maximal clique as it cannot be made any larger without losing the clique property [62]. The cliques considered in our problem are Ω_1 and Ω_2 , which represent the 1st and 2nd order neighborhood cliques respectively. Parameter β needs to be cross-validated.

By taking applying expression (22) and (23) in (21) and taking logarithms, the energy function for a pixel i with class y_i and features \mathbf{x}_i results in

$$\mathcal{E}(y_i = \mathcal{C}_k | \mathbf{x}_i, \boldsymbol{\mu}_k, \boldsymbol{\Sigma}_k) = -\frac{1}{2} \log |\boldsymbol{\Sigma}_k| - \frac{1}{2} (\mathbf{x}_i - \boldsymbol{\mu}_k)^\top \boldsymbol{\Sigma}_k^{-1} (\mathbf{x}_i - \boldsymbol{\mu}_k) + \psi(y_i). \quad (25)$$

plus constant terms, this is, one can say that $p(y_i = \mathcal{C}_k | \mathbf{x}_i, \boldsymbol{\theta}_k)$ is proportional to $\exp[\mathcal{E}(y_i = \mathcal{C}_k | \mathbf{x}_i, \boldsymbol{\theta}_k)]$. In order to find this probability, this exponential must be simply normalized, leading to the following softmax function

$$p(y_i = \mathcal{C}_k | \mathbf{x}_i, \boldsymbol{\theta}_k) = \frac{\exp \mathcal{E}(y_i = \mathcal{C}_k | \mathbf{x}_i, \boldsymbol{\theta}_k)}{\sum_{k=1}^K \exp \mathcal{E}(y_i = \mathcal{C}_k | \mathbf{x}_i, \boldsymbol{\theta}_k)}. \quad (26)$$

A class \mathcal{C}_k is assigned to the sample \mathbf{x}_i by the MAP criterion,

$$\hat{y}_i = \underset{k}{\operatorname{argmax}} p(y_i = \mathcal{C}_k | \mathbf{x}_i, \boldsymbol{\theta}_k). \quad (27)$$

Supervised Inference. In order to apply a MRF to the segmentation problem, an image is defined as a lattice graph where pixels i, j are the connection nodes of a rectangular grid that is embedded in an Euclidean space \mathbb{R}^2 . Besides of defining a pixel with a pair of coordinates in a 2D lattice, a pixel is defined as a feature vector $\mathbf{x}_{i,j}$ in a space of d dimensions. The feature process is the a set of observations $\mathcal{F} = \{\mathbf{x}_{i,j} \in \mathbb{R}^d \mid i = 1, \dots, N, j = 1, \dots, M\}$, from a random field. The hidden process of the labels $\mathcal{Y} = \{y_{i,j} \in \mathcal{C}_k \mid i = 1, \dots, N, j = 1, \dots, M\}$, is another random field of a discrete random variable, which possible outcomes are $\mathcal{C}_k \in \{-1, 1\}$ in our segmentation problem [66].

The likelihood function is approximated with multivariate normal distribution $\mathcal{N}(\boldsymbol{\mu}_k, \boldsymbol{\Sigma}_k)$ for each class \mathcal{C}_k . For a training data set with z images, the labels of the pixels are known and the parameter set $\boldsymbol{\theta}_k$ from the sample feature distribution in class \mathcal{C}_k can be estimated by ML. The sample mean is,

$$\boldsymbol{\mu}_k = \frac{1}{|\mathcal{S}_k|} \sum_{\mathbf{x}_{i,j,z} \in \mathcal{S}_k^{(t)}} \mathbf{x}_{i,j,z}, \quad (28)$$

and the sample covariance is,

$$\boldsymbol{\Sigma}_k = \frac{1}{|\mathcal{S}_k| - 1} \sum_{\mathbf{x}_{i,j,z} \in \mathcal{S}_k} (\mathbf{x}_{i,j,z} - \boldsymbol{\mu}_k) \cdot (\mathbf{x}_{i,j,z} - \boldsymbol{\mu}_k), \quad (29)$$

where $|\cdot|$ denotes the cardinality of the set of labels \mathcal{C}_k .

For a test sample, the potential function depends on the labels assigned to neighboring pixels in the cliques Ω , and assuming that the likelihood for the test sample is equal to the one for the training sample, the classification is optimized iterating such as,

$$y_{i,j}^{(t+1)} = \underset{k}{\operatorname{argmax}} \log p(\mathbf{x}_{i,j} | y_{i,j}^{(t)} = \mathcal{C}_k, \boldsymbol{\theta}_k) + \sum_{n,m \in \Omega} V_{\Omega}(y_{i,j}^{(t)}, y_{n,m}^{(t)}) \quad (30)$$

$$\forall i = 1, \dots, N, j = 1, \dots, M,$$

where t is the iteration number and $\boldsymbol{\theta}_k = \{\boldsymbol{\mu}_k, \boldsymbol{\Sigma}_k\}$. The optimization ends when a maximum in total energy function is reached $\sum_{i,j} \mathcal{E}(y_{i,j}^{(t+1)} | \mathbf{x}_{i,j}, \boldsymbol{\theta}_k)$. This means that the model has converged to a stable configuration of the hidden process of the labels.

Unsupervised Inference: Iterated Conditional Modes. The inference of the parameters set of the class distributions in a MRF model can be performed using the ICM algorithm. This algorithm is an unsupervised learning method [47].

The algorithm begins by assigning randomly a class to each pixel drawing samples from a uniform distribution $y_{i,j} \sim \mathcal{U}(0, K)$. The samples with label \mathcal{C}_k are defined within the set $S_k^{(0)}$. The algorithm iteratively updates the set of parameters $\boldsymbol{\theta}_k$ from the distribution used to approximate the feature vectors in a class. The mean of a class is the sample mean,

$$\boldsymbol{\mu}_k^{(t+1)} = \frac{1}{|S_k^{(t)}|} \sum_{\mathbf{x}_{i,j,z} \in S_k^{(t)}} \mathbf{x}_{i,j,z}, \quad (31)$$

and the covariance of a class is the sample covariance,

$$\boldsymbol{\Sigma}_k^{(t+1)} = \frac{1}{|S_k^{(t)}| - 1} \sum_{\mathbf{x}_{i,j,z} \in S_k^{(t)}} \left(\mathbf{x}_{i,j,z} - \boldsymbol{\mu}_k^{(t+1)} \right) \cdot \left(\mathbf{x}_{i,j,z} - \boldsymbol{\mu}_k^{(t+1)} \right)^T. \quad (32)$$

A class is reassigned to each pixel according to the parameters computed at iteration $t + 1$. The classification follows the MAP criteria,

$$y_{i,j}^{(t+1)} = \underset{k}{\operatorname{argmax}} \mathcal{E}(y_{i,j}^{(t)} | \mathbf{x}_{i,j}, \boldsymbol{\mu}_k^{(t+1)}, \boldsymbol{\Sigma}_k^{(t+1)}). \quad (33)$$

When the total energy stops increasing, so that $\sum_{i,j} \mathcal{E}(y_{i,j}^{(t+1)} | \mathbf{x}_{i,j}, \boldsymbol{\theta}_k^{(t+1)}) \leq \sum_{i,j} \mathcal{E}(y_{i,j}^{(t)} | \mathbf{x}_{i,j}, \boldsymbol{\theta}_k^{(t)})$, the algorithm has converged to a stable configuration and the optimal set of parameters $\boldsymbol{\theta}_k$ have been found. The distribution of class \mathcal{C}_k is defined as $\mathcal{N}(\boldsymbol{\mu}_k^{(t)}, \boldsymbol{\Sigma}_k^{(t)})$.

Simulated Annealing. The standard optimization goes through all the pixels calculating their potential and classifying them in each iteration of the algorithm. The computational cost of this method is high, but we can assume that it is not necessary to evaluate the pixels whose state has high energy, because their classification will not change. The computation cost can be reduced by sampling the pixels that are likely to be misclassified, and applying the optimization procedure only to them.

We propose to optimize the configuration of the pixels in an IR image applying the Simulated Annealing algorithm (SA) [67] to the MRF models [66]. SA algorithm is applied on the implementation, after the inference of the class distributions.

The class distributions $\mathcal{N}(\boldsymbol{\mu}_k, \boldsymbol{\Sigma}_k)$ were previously inferred applying a supervised or unsupervised learning algorithm. The optimization is initialized to ML classification of the pixels,

$$y_{i,j}^{(0)} = \underset{k}{\operatorname{argmax}} p(y_{i,j} = \mathcal{C}_k | \mathbf{x}_{i,j}, \boldsymbol{\theta}_k). \quad (34)$$

The likelihood a pixel to belong a class \mathcal{C}_k is only evaluated at the initialization of the algorithm.

The objective is to evaluate the potential function of the samples that have low energy. For that, a sample $\mathbf{x}_{i,j}$ with label $y_{i,j} = \mathcal{C}_k$ is randomly selected and its classification is changed in each iteration t , so that $\bar{y}_{i,j}^{(t)} = 1 - y_{i,j}^{(t)}$. The probability of selecting a sample $\mathbf{x}_{i,j}$ is weighted by their energy. The weights of the samples in an image are defined as,

$$w_{i,j} = \frac{\mathcal{E}(\bar{y}_{i,j}^{(t)} | \mathbf{x}_{i,j}, \boldsymbol{\theta}_k) - \max_k \mathcal{E}(\bar{y}_{i,j}^{(t)} | \mathbf{x}_{i,j}, \boldsymbol{\theta}_k)}{\sum_{i,j} [\mathcal{E}(\bar{y}_{i,j}^{(t)} | \mathbf{x}_{i,j}, \boldsymbol{\theta}_k) - \max_k \mathcal{E}(\bar{y}_{i,j}^{(t)} | \mathbf{x}_{i,j}, \boldsymbol{\theta}_k)]}, \quad (35)$$

and the cumulative distribution of the weights is computed such as $\bar{w}_{n,m} = \{\{\sum_{i=1}^n \sum_{j=1}^m w_{i,j}\}_{n=1}^N\}_{m=1}^M$. Then, a sample is drawn from a uniform distribution $\hat{w} \sim \mathcal{U}(0, 1)$. The sample whose weight has the minimum distance to the drawn sample, is selected $i, j = \operatorname{argmin} |\bar{w}_{i,j} - \hat{w}|$.

The algorithm follows with Metropolis step which is computed with the energy of the changed sample $\bar{y}_{i,j}$ and the energy of the original label $y_{i,j}$,

$$\Delta E = \mathcal{E} \left(y_{i,j}^{(t)} \mid \mathbf{x}_{i,j}, \boldsymbol{\theta}_k \right) - \mathcal{E} \left(\bar{y}_{i,j}^{(t)} \mid \mathbf{x}_{i,j}, \boldsymbol{\theta}_k \right). \quad (36)$$

The new label is directly accepted $\bar{y}_{i,j}^{(t)}$ iff $\Delta E < 0$. Otherwise, it will be accepted with probability $\rho = \exp(-\Delta E/T^{(t)})$ in an analogous way to thermodynamics with the Gibbs distribution,

$$y_{i,j}^{(t+1)} = \begin{cases} \bar{y}_{i,j}^{(t)} & \text{if } \Delta E \leq 0 \\ \bar{y}_{i,j}^{(t)} & \text{if } \Delta E > 0 \text{ and } \rho > u \\ y_{i,j}^{(t)} & \text{Otherwise} \end{cases} \quad (37)$$

the acceptance probability is drawn from a uniform distribution $u \sim \mathcal{U}(0, 1)$.

We propose to linearly cool down the acceptance rate through the temperature parameter, so that $T^{(t+1)} = \alpha T^{(t)}$. The optimal parameter α is a trade off between accuracy and speed.

3.2 Discriminative Models

In these supervised models, the training samples are utilized to infer a function that maps each vector of features to a label pair. A polynomial expansion is applied to the vector of features, that were extracted from a neighborhood structure of pixels, in order to model a non-linear relation between features and the label. The function is directly found in the RR via regularized LS, whilst the functional in our implementation of the linear SVC is solved by gradient descent, as well as the negative marginal log-likelihood in the linear GP. The reason for the necessity of solving the optimizations in a primal space is due to the fact that a solution in a dual space requires manipulating matrices of dimensions $N \times N$, where N is the number of training data, which in the present application makes the computational burden hardly tractable. However, when the used Hilbert space is of finite dimension, the problem becomes tractable and efficient.

A polynomial expansion is applied so the number of dimensions in the projection space is finite. This allow us to solve the problem in the primal formulation. The polynomial expansion of the covariates is defined as $\varphi : \mathcal{X} \mapsto \mathcal{P}^n$, where n is the order of the expansion. The dimensions in the output space is given by $\mathcal{P}^n = [(n + (d - 1))!]/[n!(d - 1)]$, so when the transformation is applied to a covariate vector $\mathbf{x}_i \mapsto \varphi(\mathbf{x}_i)$, a vector is expanded to this \mathcal{P}^n -dimension space $\varphi(\mathbf{x}_i) \in \mathbb{R}^{\mathcal{P}^n}$. The polynomial expansion of the dataset $\mathcal{D} = \{\Phi, \mathbf{y}\}$, is defined matrix form as,

$$\Phi = \begin{bmatrix} \varphi(\mathbf{x}_1) \\ \vdots \\ \varphi(\mathbf{x}_N) \end{bmatrix}, \quad \Phi \in \mathbb{R}^{N \times \mathcal{P}^n}, \quad \mathbf{y} = \begin{bmatrix} y_1 \\ \vdots \\ y_N \end{bmatrix}, \quad (38)$$

where $y_i \in \{0, 1\}$ that are labels for a clear or cloudy pixel respectively.

3.2.1 Ridge Regression

The RR is a Minimum Mean Squared Error (MMSE) method with quadratic norm regularization applied on the parameters \mathbf{w} ,

$$\min_{\mathbf{w}} \sum_{i=1}^N (\mathbf{y} - \mathbf{w}^\top \Phi)^2 + \gamma \cdot \|\mathbf{w}\|_2. \quad (39)$$

where γ is the regularization parameter, and it has to be cross-validated. As a polynomial expansion is used, RR can be solved in the primal.

The parameters \mathbf{w} that minimize loss function are analytically found applying Least-Squares (LS),

$$\begin{aligned} 0 &= \frac{\partial}{\partial \mathbf{w}} \cdot \left[(\mathbf{y} - \mathbf{w}^\top \Phi)^\top (\mathbf{y} - \mathbf{w}^\top \Phi) + \gamma \cdot \operatorname{tr}(\mathbf{w}^\top \mathbf{w}) \right] \\ 0 &= 2 \cdot [\Phi^\top (\Phi \mathbf{w} - \mathbf{y}) + \gamma \cdot \mathbf{w}] \\ \bar{\mathbf{w}} &= (\Phi^\top \Phi + \gamma \cdot \mathbf{I})^{-1} \Phi^\top \mathbf{y}. \end{aligned} \quad (40)$$

In this case, as the model is for classification, a sigmoid function is applied to the prediction,

$$\begin{aligned} p(\mathcal{C}_1 \mid \varphi(\mathbf{x}_*), \mathcal{D}) &= \frac{1}{1 + \exp(-\bar{\mathbf{w}}^\top \varphi(\mathbf{x}_*))} \\ p(\mathcal{C}_2 \mid \varphi(\mathbf{x}_*), \mathcal{D}) &= 1 - p(\mathcal{C}_1 \mid \varphi(\mathbf{x}_*), \mathcal{D}). \end{aligned} \quad (41)$$

The result is probability between 0 and 1. The classification threshold is initially set to 0.5, thus the class with higher probability is the predicted class. Lately, it is explained the method implemented to cross-validate the threshold, so that the different models have the same objective function.

3.2.2 Primal solution for Support Vector Machines

We propose to solve a SVC for binary classification in the primal to limit the complexity of the model for cloud segmentation due to the large number of pixels samples [68, 69, 70], so that only dot product kernels are feasible. The formulation of the unconstrained optimization problem for a dataset that is $\mathbf{X} = \{\mathbf{x}_i \in \mathbb{R}^D \mid \forall i = 1, \dots, N\}$, and $\mathbf{y} = \{y_i \in \{-1, +1\} \mid \forall i = 1, \dots, N\}$ is,

$$\min_{\mathbf{w}} \frac{1}{2} \|\mathbf{w}\| + C \sum_{i=1}^N \xi(\mathbf{w}; \mathbf{x}_i, y_i) \quad (42)$$

where $C > 0$ is the penalty term, $\xi(\mathbf{w}; \mathbf{x}_i, y_i)$ is the loss function, and in our model the norm is a L_2 , so we have

$$\min_{\mathbf{w}} \frac{1}{2} \|\mathbf{w}\|_2 + C \sum_{i=1}^N \left(\max[0, 1 - y_i \mathbf{w}^\top \varphi(\mathbf{x}_i)] \right)^2, \quad (43)$$

which is a Maximum Margin (MM) problem [69]. The complexity parameter C has to be cross-validated.

The original formulation of the linear SVC, do have not a probabilistic output. However, the distance from a sample to the hyper-plane can be transformed to a probability measure,

$$\begin{aligned} p(\mathcal{C}_1 \mid \varphi(\mathbf{x}_*), \mathcal{D}) &= \frac{1}{1 + \exp(-\bar{\mathbf{w}}^\top \varphi(\mathbf{x}_*))} \\ p(\mathcal{C}_2 \mid \varphi(\mathbf{x}_*), \mathcal{D}) &= 1 - p(\mathcal{C}_1 \mid \varphi(\mathbf{x}_*), \mathcal{D}), \end{aligned} \quad (44)$$

using the sigmoid function, similarly to the proposed RR for classification.

3.2.3 Primal solution for Gaussian Processes

A GP when is formulated in the primal is known as Bayesian logistic regression [62, 71, 72]. In contrast to Bayesian linear regression, this approach has not an analytical solution,

$$p(\mathbf{w} \mid \mathcal{D}) \propto p(\mathbf{y} \mid \Phi, \mathbf{w}) \cdot p(\mathbf{w}). \quad (45)$$

The likelihood function of the model is $p(y_i \mid \Phi, \mathbf{w}) = \prod_{i=1}^N \hat{y}_i^{y_i} (1 - \hat{y}_i)^{1-y_i}$, where $\hat{\mathbf{y}} = [\hat{y}_1 \dots \hat{y}_N]^\top$ are the predictions. The prior is Gaussian $p(\mathbf{w}) \sim \mathcal{N}(\mathbf{w} \mid \mu_0, \Sigma_0)$, so that the posterior is not Gaussian. The Laplace approximation is applied to assume that the posterior is Gaussian $q(\bar{\mathbf{w}}) \sim \mathcal{N}(\bar{\mathbf{w}} \mid \bar{\mathbf{w}}, \Sigma_n)$.

The optimal set of parameters are found maximizing the marginal log-likelihood via numerical gradient,

$$\begin{aligned} \log p(\mathbf{w} \mid \mathcal{D}) &= -\frac{d}{2} \log 2\pi - \frac{1}{2} \log |\Sigma_0| - \frac{1}{2} (\mathbf{w} - \mu_0)^\top \Sigma_0^{-1} (\mathbf{w} - \mu_0) + \\ &+ \sum_{i=1}^N [y_i \log \hat{y}_i + (1 - y_i) \log (1 - \hat{y}_i)], \end{aligned} \quad (46)$$

where $\hat{y}_i = \sigma(\mathbf{w}^\top \varphi(\mathbf{x}_i)) = 1/[1 + \exp(-\mathbf{w}^\top \varphi(\mathbf{x}_i))]$, which is the sigmoid function.

The posterior covariance is the inverse of the Hessian of the negative log-posterior,

$$\Sigma_n^{-1} = \Sigma_0^{-1} + \sum_{i=1}^N y_i (1 - y_i) \varphi(\mathbf{x}_i) \varphi(\mathbf{x}_i)^\top. \quad (47)$$

Since the convolution of a sigmoid with a Gaussian is untractable, the sigmoid is approximated by a probit function. The approximation of the predictive distribution is,

$$\begin{aligned} p(C_1 | \mathcal{D}) &= \int \sigma(\alpha) \cdot \mathcal{N}(\alpha | \mu_\alpha, \sigma_\alpha) d\alpha \\ &\approx \sigma(\Phi(\sigma_\alpha) \cdot \mu_\alpha), \end{aligned} \quad (48)$$

where $\alpha = \bar{\mathbf{w}}^\top \Phi$. The predictive mean is $\mu_\alpha = \bar{\mathbf{w}}^\top \Phi$, and the variance is $\sigma_\alpha^2 = \Phi^\top \Sigma_n \Phi$. The probit approximation of a sigmoid is $\Phi(\sigma_\alpha) = (1 + \sigma_\alpha \pi / 8)^{-1/2}$. The probability of the C_2 is computed as,

$$p(C_2 | \varphi(\mathbf{x}_*), \mathcal{D}) = 1 - p(C_1 | \varphi(\mathbf{x}_*), \mathcal{D}). \quad (49)$$

4 J-Statistic

The Younde's j-statistic or Younde's Index is a test to evaluate the performances of a binary classification [73], that is defined as,

$$J = sensitivity + specificity - 1. \quad (50)$$

The entries on the confusion matrix are used to compute the sensitivity,

$$sensitivity = \frac{TP}{TP + FN}, \quad (51)$$

where TP and FN are the true positives and false negatives, and the specificity is,

$$specificity = \frac{TN}{TN + FP}, \quad (52)$$

where TN and FP are the true negatives and false positives. It is different to the accuracy score of a binary classification, which is also obtained using the entries of the confusion matrix, and that it is,

$$ACC = \frac{TP + TN}{TP + FP + TN + FN}. \quad (53)$$

As the optimized loss function is different in each model, we propose to define a prior λ , which has to be cross-validated for each one of models, and has an optimal value for each classification function,

$$\begin{aligned} p(\mathcal{D} | \mathcal{C}_k) &= \frac{p(\mathcal{C}_k | \mathcal{D}) \cdot p(\mathcal{C}_k)}{p(\mathcal{D})} \\ &\propto p(\mathcal{C}_k | \mathcal{D}) \cdot p(\mathcal{C}_k) \\ &\propto p(\mathcal{C}_k | \mathcal{D}) \cdot \lambda \end{aligned} \quad (54)$$

so the maximized loss function is the same in all the models. The classification probabilities are defined as $p(\mathcal{D} | \mathcal{C}_1) = p(\mathcal{C}_1 | \mathcal{D}) \cdot \lambda$, and $p(\mathcal{D} | \mathcal{C}_2) = 1 - p(\mathcal{D} | \mathcal{C}_1)$. The j-statistic score is maximized finding the optimal binary classification λ threshold. For that, the j-statistic is applied to the conventional Receiver Operating Characteristic (ROC) analysis [74], and it is computed at each point of the ROC. We propose to use the maximum value of j-statistic in the ROC curve as the optimal point.

After the cross-validation of the virtual prior λ , a class \mathcal{C}_k is assigned to a sample \mathbf{x}_* following this criteria,

$$\hat{y}_* = \underset{k}{\operatorname{argmax}} p(\mathcal{C}_k | \mathbf{x}_*, \mathcal{D}) \cdot \lambda, \quad (55)$$

that is just a MAP estimation.

5 Experiments

The proposed segmentation methods utilize data acquired by an innovative system, which captures circumsolar IR images at the same time that measures global horizontal irradiance using a pyranometer [54]. The DAQ is equipped with a solar tracker that updates its pan, and tilt every second, maintaining the Sun in a central position in the images along a day. The IR sensor is a Lepton¹ camera with radiometry which has a wavelength from 8 to 14 micros, and

¹<https://www.flir.com/>

provides an uniform thermal image as the output. When the radiometry functionality is enabled, the pixels in a frame are turned into temperature measurements in centikelvin units. The resolution of an IR image is 80×60 pixels. The DAQ is localized on the roof area of UNM-ME building in Albuquerque, NM.

The weather features that were used to compute the clouds height as well as to remove cyclostationary artifacts on the IR images are: atmospheric pressure, air temperature, dew point and humidity. The weather station is set to measure every 10 minutes, so the data was interpolated to match the IR images sampling interval. The weather station is located at the University of New Mexico Hospital, and both its real-time and historical data are publicly accessible².

The database of IR images has one year of day samples. Each day sample contains IR images recorded every 15 seconds during daylight. The samples were randomly selected to form the data set used in the cross-validation of the segmentation models. The data set is composed of 12 images with their labels, it amounts for a total of 57,600 pixels. The samples belong to different days in all four seasons. They are organized chronologically and divided into training (earlier dates) and testing set (later dates). The training set has 7 images, which has 33,600 pixels in total. The testing set has the remaining 5 images, which has 24,000 pixels. The training set contains 5 images with clouds, 1 image with clear-sky, and another one with covered sky. The testing set has 3 images with clouds, 1 images with clear-sky, and 1 with covered sky.

The pixels in the images that form the data set, were manually labelled as clear $y_{i,j} = 0$ or cloudy pixel $y_{i,j} = 1$. The feature of reference to perform the labelling was temperatures $T_{i,j}$ of the pixels. The temperature in the background of the images varies across the year. This background temperature is the temperature of the Tropopause. For each image, this temperature is first identify, and then used as a reference to distinguish which pixels have a temperature different of the background temperature. The entries of matrix (with the dimension of the original IR image) are set to 0 if there is background, or to 1 if there is a cloud.

The Leave-One-Out (LOO) method is implemented in the cross-validation of the parameters. In this method, the training samples are left out for validation one at a time, whilst the rest of the training samples are used to fit the model. The model is fitted for a set of hyperparameters and a virtual prior λ parameter in Eq. (54). The virtual prior is adjusted to the optimal j-statistic using the predicted probabilities of each class for each combination of hyperparameter that is cross-validated. The virtual prior λ is cross-validated in all the models. The validation j-statistic is the average of the j-statistics obtained in each one of the LOO cross-validation loops. The model selection criteria is best j-statistic in the validation set.

In the generative models, NBC and k-means clustering have not hyperparameters. GDA and GMM have the covariance matrix regularization term γ which has to be cross-validated in Eq. (2) and (10) respectively. In the k-means clustering, the features were standardized as $\bar{\mathbf{x}}_{i,j} = [\mathbf{x}_{i,j} - \mathbf{E}(\mathbf{X})]/\text{Var}(\mathbf{X})$ in each one of the feature vectors. The rest of the models did not required normalization nor standardization of the feature vectors.

In the MRF models, the parameter of cliques β in Eq. (24) was cross-validated in all the models. The supervised MRF have the covariance matrix regularization term γ of in Eq. (25) which was cross-validated. The unsupervised MRF with ICM algorithm is computationally expensive, so the regularization term of the covariance matrix was set fixed to $\gamma = 1$. In the supervised MRF with SA in the implementation, the cross-validated parameters were the regularization term of the covariance matrix γ , and the cooling parameters α of the SA algorithm in Eq. (37). The unsupervised MRF with ICM algorithm in the inference and SA algorithm in the implementation, the regularization term of the covariance matrix was set fixed to $\gamma = 1$, and cooling parameters of the SA algorithm was set fixed to $\alpha = 0.75$.

In the discriminate models, the RR has the regularization γ of LS solution in Eq. (39) that has to be cross-validated. The SVC has the complexity term C of the loss function in Eq. (43). The hyperparameters of the GP are the prior mean μ_0 and covariance matrix Σ_0 . The prior mean and covariance matrix in Eq. (46) are simplified to $\mu_0 \triangleq \mathbf{0}$ and $\Sigma_0 \triangleq \mathbf{I}_{D \times D} \cdot \gamma$, so only the parameter γ is cross-validated.

The experiments were carried out in the Wheeler high performances computer of UNM-CARC, which uses SGI AltixXE Xeon X5550 at 2.67GHz with 6 GB of RAM memory per core, has 8 cores per node, 304 nodes total, and runs at 25 theoretical peak FLOPS. It has installed Linux CentOS 7.

6 Discussion

The performances of the selected models are evaluated using the test set. The generative models that achieved the best test j-statistic were the MRFs. The best generative model without a potential function was discriminant analysis. GDA achieved the best j-statistic when implemented with the feature vector \mathbf{x}^4 of a 2^{nd} order neighborhood (see Fig.

²<https://www.wunderground.com/dashboard/pws/KNMALBUQ473>

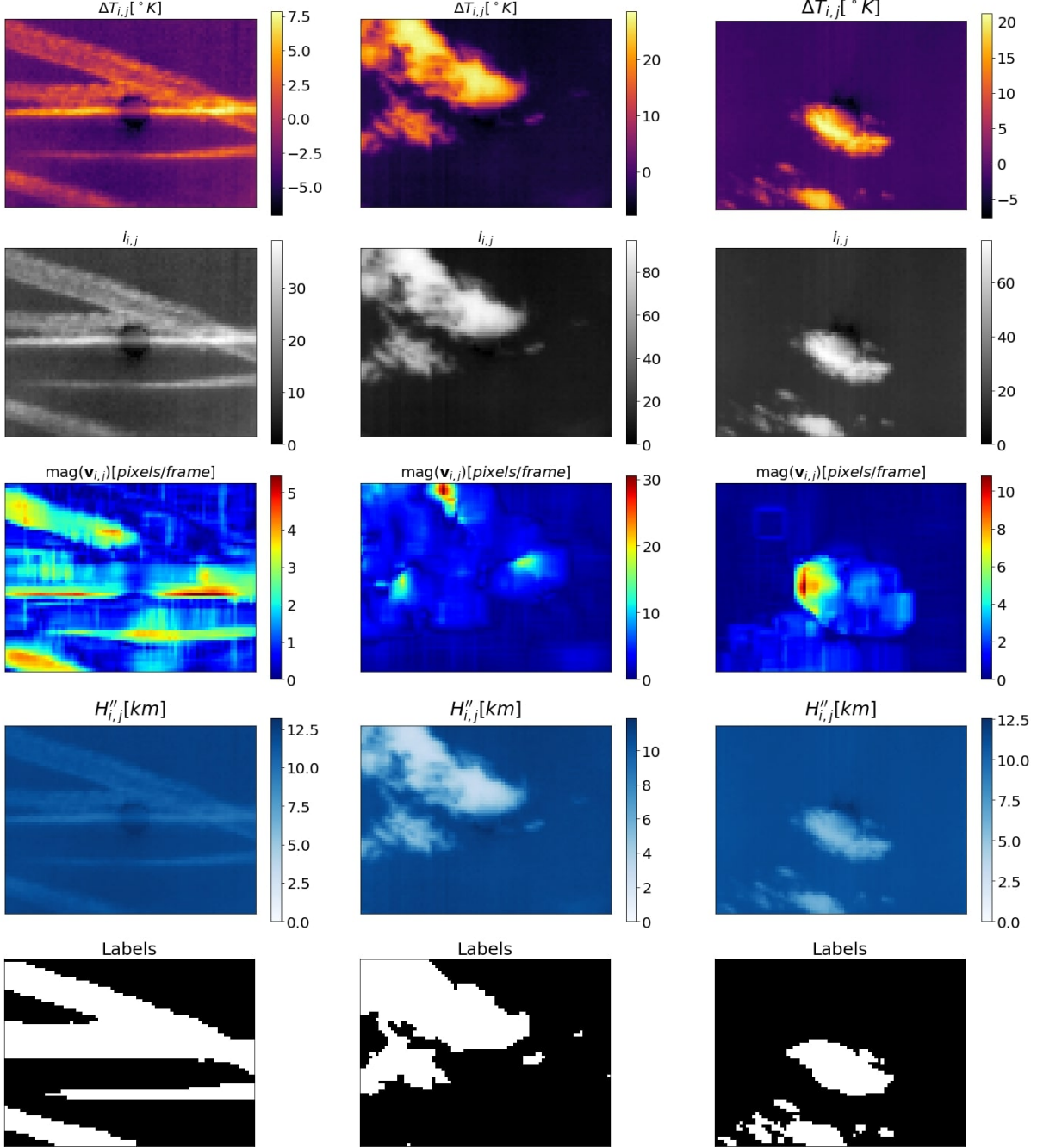


Figure 1: This figure shows the features extracted from three test images. The test images are organized in columns. The images in the first row show the normalized intensity of the pixels. The images in the second row show the magnitude of the velocity vectors. The images in the third row show the increments of temperature with respect to the height of the Tropopause. The images in the fourth row show the heights of the clouds. The last row shows the test images in which the clouds were manually segmented.

2). When a trade-off between average testing time and j-statistic is considered, the most suitable model is the GMM using the feature vector \mathbf{x}^4 of a single pixel. The Fig. 4 shows the j-statistics obtained by the discriminative models using a polynomial expansion. The best model was the GP solved in the primal, when a polynomial expansion is not applied to the feature vectors. The feature vector was \mathbf{x}^4 of a single pixel. The unsupervised MRF model achieved the best j-statistic test among all the models. The ICM-MRF model used the feature vector \mathbf{x}^3 of 1st order neighborhood.

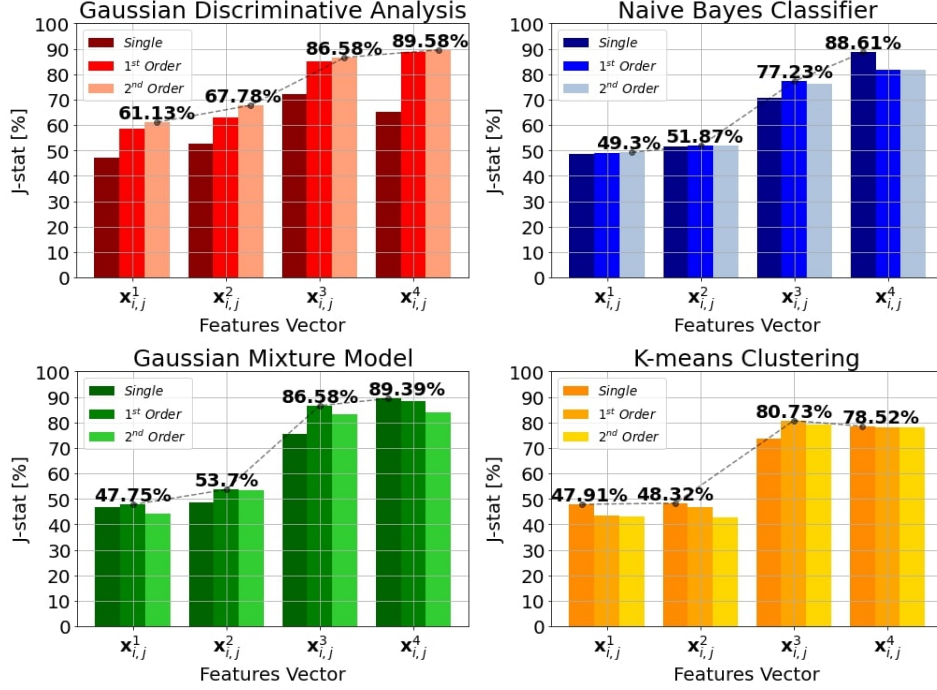


Figure 2: The graph shows the j-statistic achieved by generative models. The color of the bars in the graph indicates the order of neighborhood from dark to light. The neighborhoods are organized from the left to right within the groups of bars. This corresponds with the order of the feature vectors used in the model.

The best set of cliques was Ω_1 . The performances of the same model decreased when optimized using SA in the implementation. However, the average testing time is faster, see in Fig. 3.

Polynomial expansion of the feature vectors used in the discriminate models yields over-fitting. The best j-statistic of a discriminate model was achieved by GP. The lowest average computing time segmenting a new image was reached by the RR model, see Fig. 5.

The performances of the best models are compared in terms of j-statistic vs. training computing time and vs. average computing time in testing. The j-statistic is evaluated with the images in the test subset. The computing time is measured in seconds. The time in the y-axes of the graphs shown in Fig. 5 are displayed in logarithmic scale. The best j-statistic is achieved by the unsupervised MRF, but the training and the average testing computing time are the largest. NBC and RR have the lowest training times. In the implementation, the k-means, NBC and RR have the lowest computing time. If we have considered all of these facts, the most suitable model would be a discriminate model.

The segmentation of three test images performed by the generative models is shown in Fig. 5-7. NBC and GDA are both discriminate analysis models and supervised learning methods (see Fig. 6). The clustering models, which are k-means and GMM, are unsupervised learning methods. These are shown in Fig. 6. MRF and SA-MRF are supervised learning models and ICM-MRF and SA-ICM-MRF are unsupervised learning models. The SA algorithm is implemented to speed-up the convergence of the MRF and the ICM-MRF models. When MRF or ICM-MRF uses SA, the segmentation is not so uniform (see Fig. 7). The cooling mechanism in the Eq. (37) of the SA algorithm ends the optimization before the segmentation has converged to a state of higher energy. RR, SVC and GP are discriminate models (see Fig. 8). These were solved in the primal formulation so their performances are feasible for real-time cloud segmentation (see Fig. 5). When the Pareto front criteria is applied [75], RR and SVC are the most suitable methods. They require low training time, plus they are capable of performing accurate and fast segmentation.

The above results show the importance of feature extraction in cloud image segmentation. When using a radiometric IR camera, physical features may be extracted from the images. Processing the IR images to remove the effects of debris in the camera's window improved the performance with respect to raw radiometric IR images. In addition, removing the cyclostationary effects of the radiation from the Sun and the atmosphere yielded an improvement in the performances of the models. When the magnitude of velocity vectors are included in the feature vectors, combined with temperature increments and normalized temperature increments, the segmentation models achieved higher j-statistic. The addition of features from neighboring pixels to the features vectors improved the performances in some of the models.

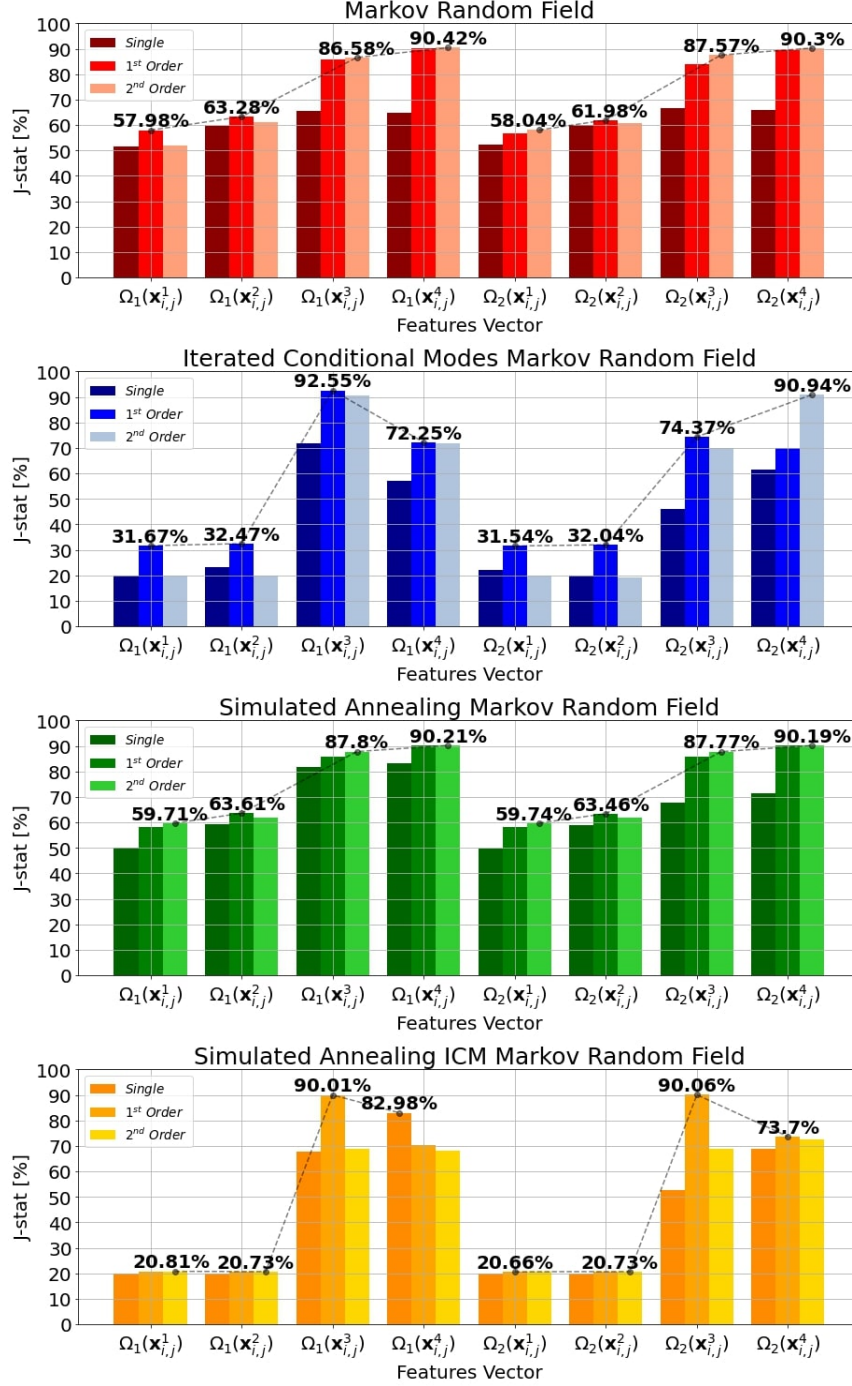


Figure 3: This figure shows the j-statistics archived by the MRFs using different cliques in their potential function. The four feature vectors are organized in groups of three bars. There are two groups of feature vectors: those with a potential function of 1st order cliques $\Omega_1(\cdot)$, and those with a potential function of 2nd order cliques $\Omega_2(\cdot)$.

When the raw temperature and height are used, all models have poor performance. However, when the images are processed with the window model and the atmospheric model, ICM-MRF reaches a reasonable performance of 92.55 % at the expense of a high computational cost of 641 ms per image in testing. The performances of discriminative methods with this set of features is lower, ranging between 72.58 % and 84 %. When velocity vectors are added to the features, then the discriminative methods reach a performance competitive with the ICM-MRF with computational times of 2.2 ms (RR), 3.7 ms (SVC) and 77 ms (GP). The best trade off is SVC, which is 150 times faster than ICM-MRF with a

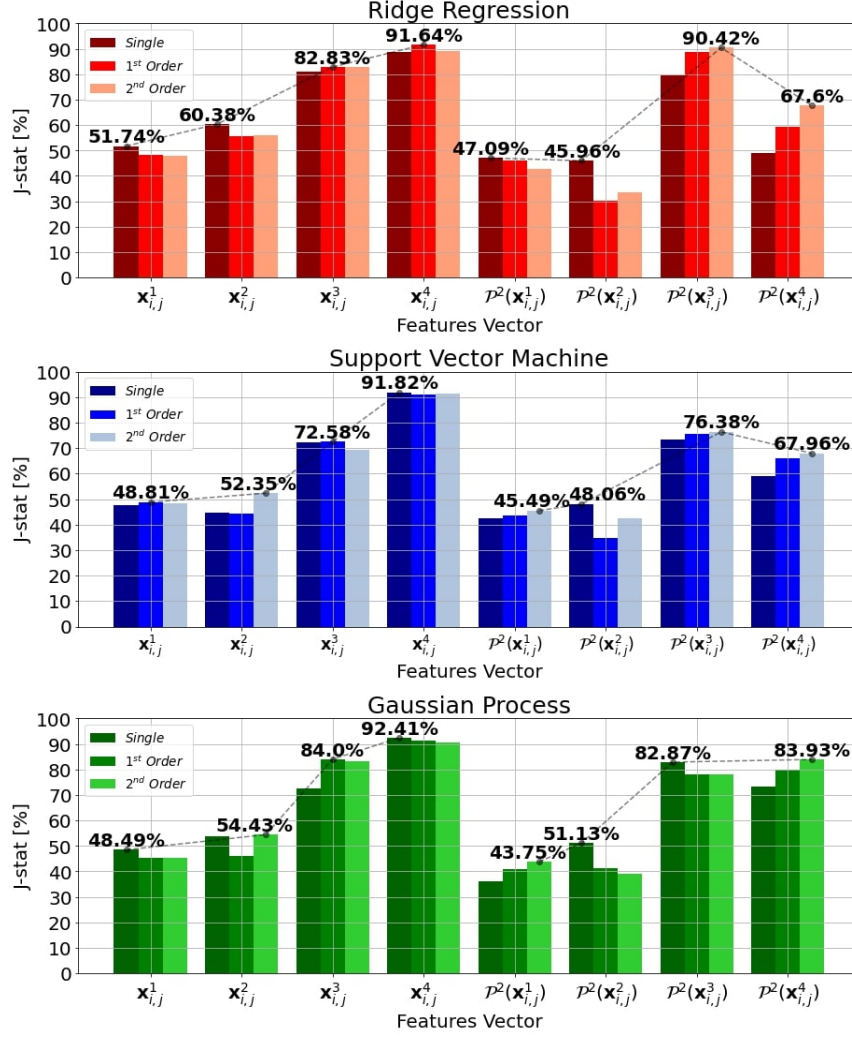


Figure 4: These graphs show the j-statistics achieved by the discriminate models. The feature vectors are organized in groups. The bars in the same group from dark to light are, respectively, features extracted from a single pixel, a 1st order neighborhood and a 2nd order neighborhood. When a polynomial expansion of second order is applied to the feature vectors, it is denoted as $\mathcal{P}^2(\cdot)$.

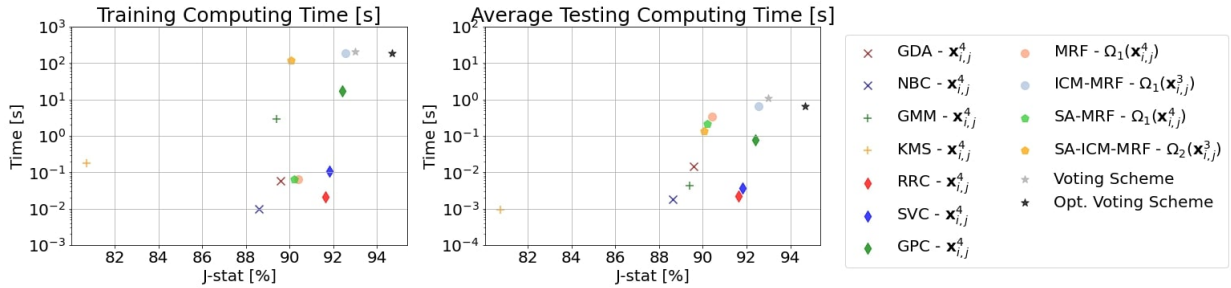


Figure 5: The graph on the left shows the computing time of each model during the training. The graph on the right shows the average computing time of each model performing the segmentation of the images in the test subset. The legend displays the optimal feature vectors, neighborhood order, polynomial expansion and cliques of each model.

small difference in accuracy. The segmentation time has to be added to the image preprocessing and feature extraction time, which is 0.1 ms for \mathbf{x}^1 , 4.7 ms for \mathbf{x}^2 , 99.9 ms for \mathbf{x}^3 and 1079 ms for \mathbf{x}^4 . This leads to the conclusion that

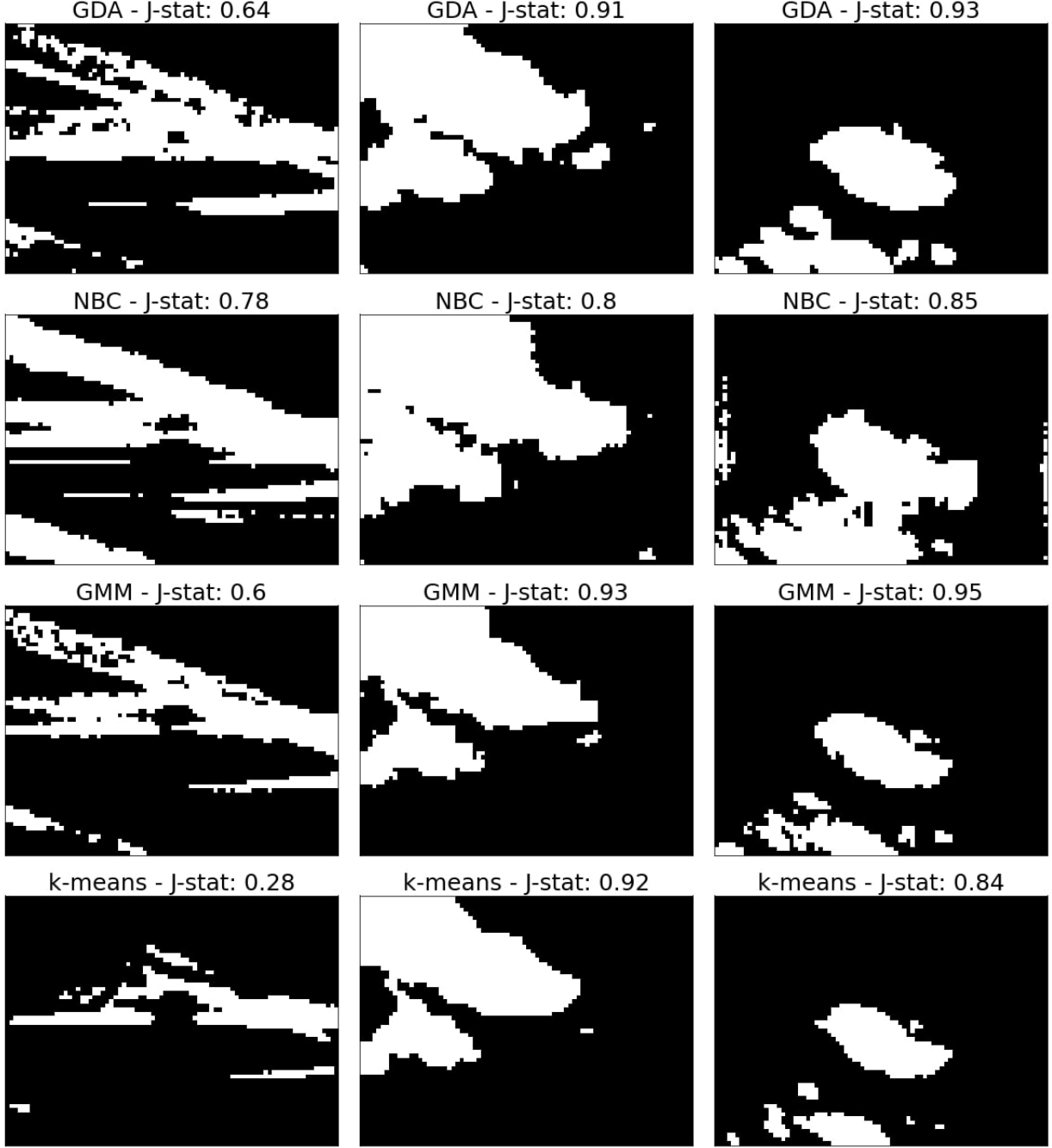


Figure 6: The figure shows three images from the test subset organized in columns. The rows are the segmentation performed by the generative models. The j-stat is the score that the method achieved in the test image. The higher j-statistic in segmenting the images was achieved by: NBC in the first image, and GMM in the second and third image.

the total average time required by ICM-MRF is 740.9 ms, which is faster than the total average time required by the discriminate models which are 1081 ms (RR), 1083 ms (SVC) and 1156 ms (GP).

A voting scheme using the predictions from the best models (not including SA-MRF and SA-ICM-MRF) achieved higher j-statistic but had a higher computing time. The achieved test j-statistic is 93 %, see Fig. 9. The combination of methods that leads to the best j-statistics is RR, SVC and ICM-MRF. This is the optimal voting scheme that reaches a j-statistic of 94.68 % in testing (see Fig. 9). The voting scheme's training and testing times are the sum of each

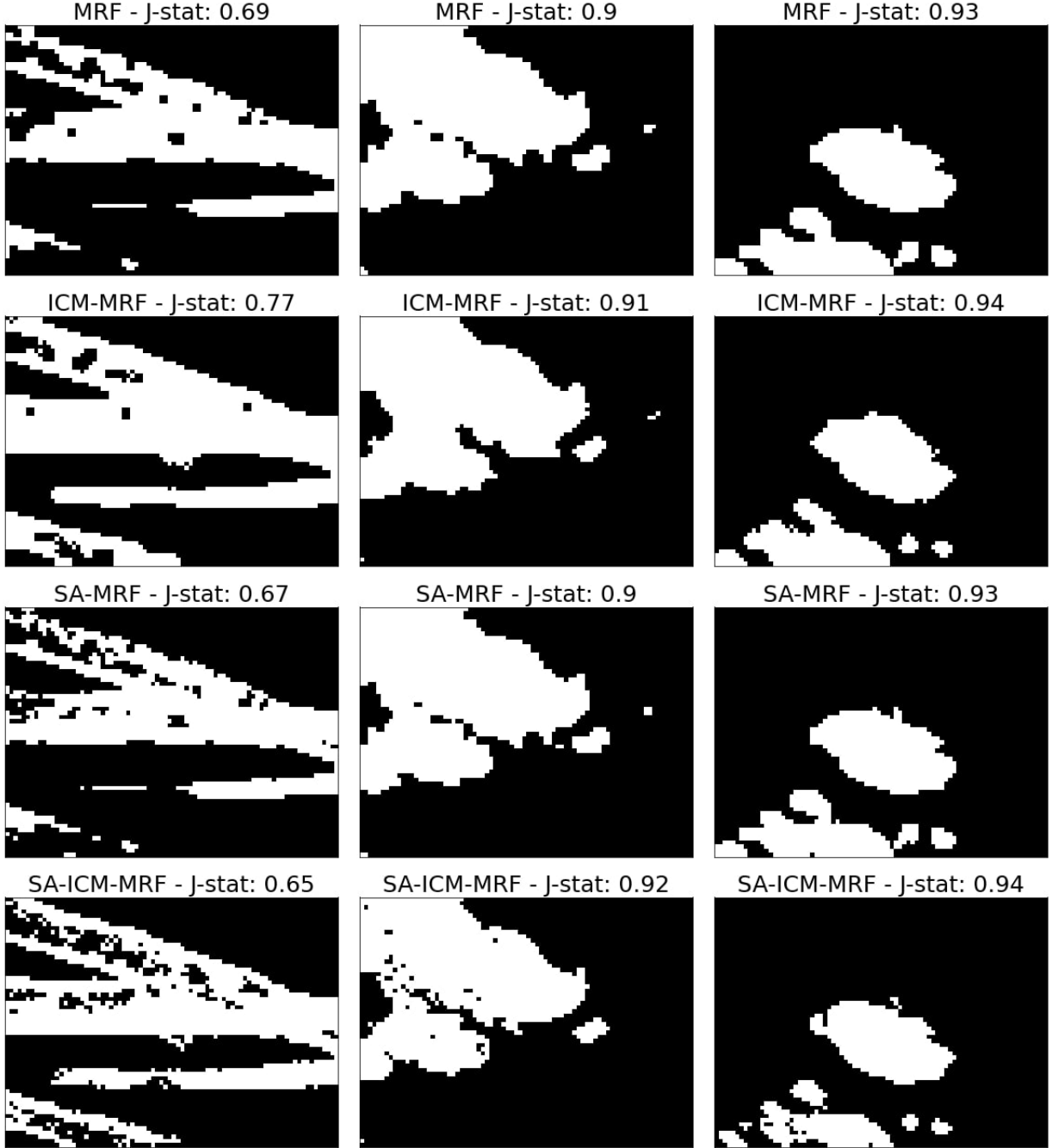


Figure 7: The figure shows three images from the test subset organized in columns. The rows are the segmentation performed by the discriminate models. The j-stat is the score that the method achieved in the test image. The higher j-statistic in segmenting the images was achieved by: ICM-MRF in the first image, SA-ICM-MRF in the second, and ICM-MRF and SA-ICM-MRF in the third image.

method's respective computing times. When the models are trained and tested in parallel, the voting scheme's training and testing times are these of the slower models.

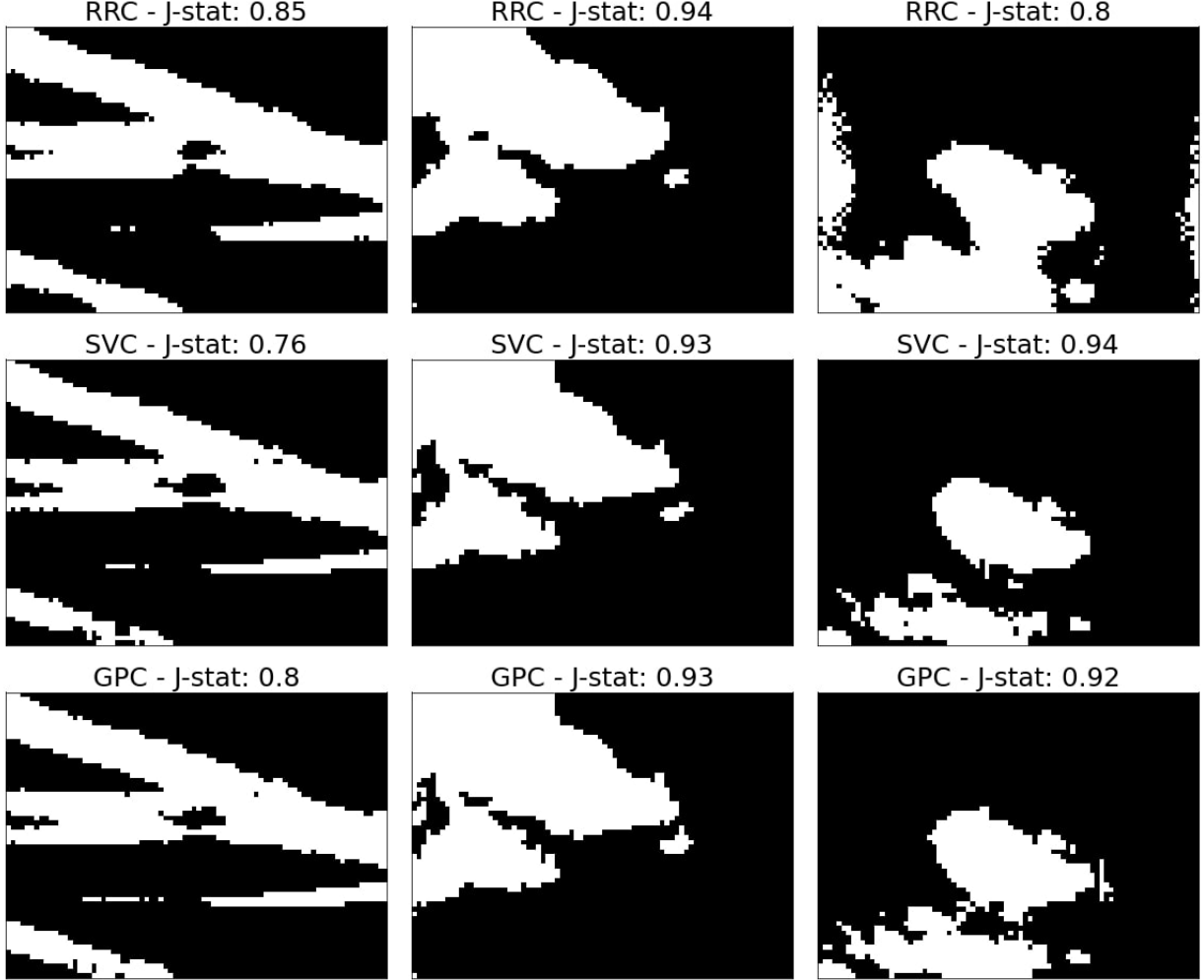


Figure 8: The figure shows three images from the test subset organized in columns. The rows are the segmentation performed by the discriminate models. The j-stat is the score that the method achieved in the test image. The higher j-statistic in segmenting the images was achieved by: RR in the first and second image, and SVC in the third image.

7 Conclusion

The objective of this research is to find an optimal method for real-time cloud segmentation in IR images, taking advantage of image preprocessing and feature extraction to produce a high performance with low computational burden. The preprocessing was used to remove underlying cycle-stationary processes, and feature extraction was used to compute cloud height and velocity. The results show that cloud segmentation in IR images is feasible with high performances in real-time applications. IR cameras perform better than visible light cameras in poor light conditions. This research implements a preprocessing algorithm that uses physical features extracted from IR images. The j-statistic is proposed as a classification metric, which independently measures the accuracy of the classification in each one of the classes.

The performances of generative and discriminate models are compared. The generative models include both supervised and unsupervised learning algorithms. The performance of the algorithms are evaluated with a simplified and full covariance matrix, and with features extracted from neighboring pixels added to the feature vectors. In the discriminate models, the performances are evaluated in the primal formulation to reduce the computational time. In this way, the discriminate models are feasible in real-time applications. Finally, the generative models are subdivided into MRF models. The prior functions of these models are cliques. The cliques are a graphical model that produces a classification using the labels of neighboring pixels.

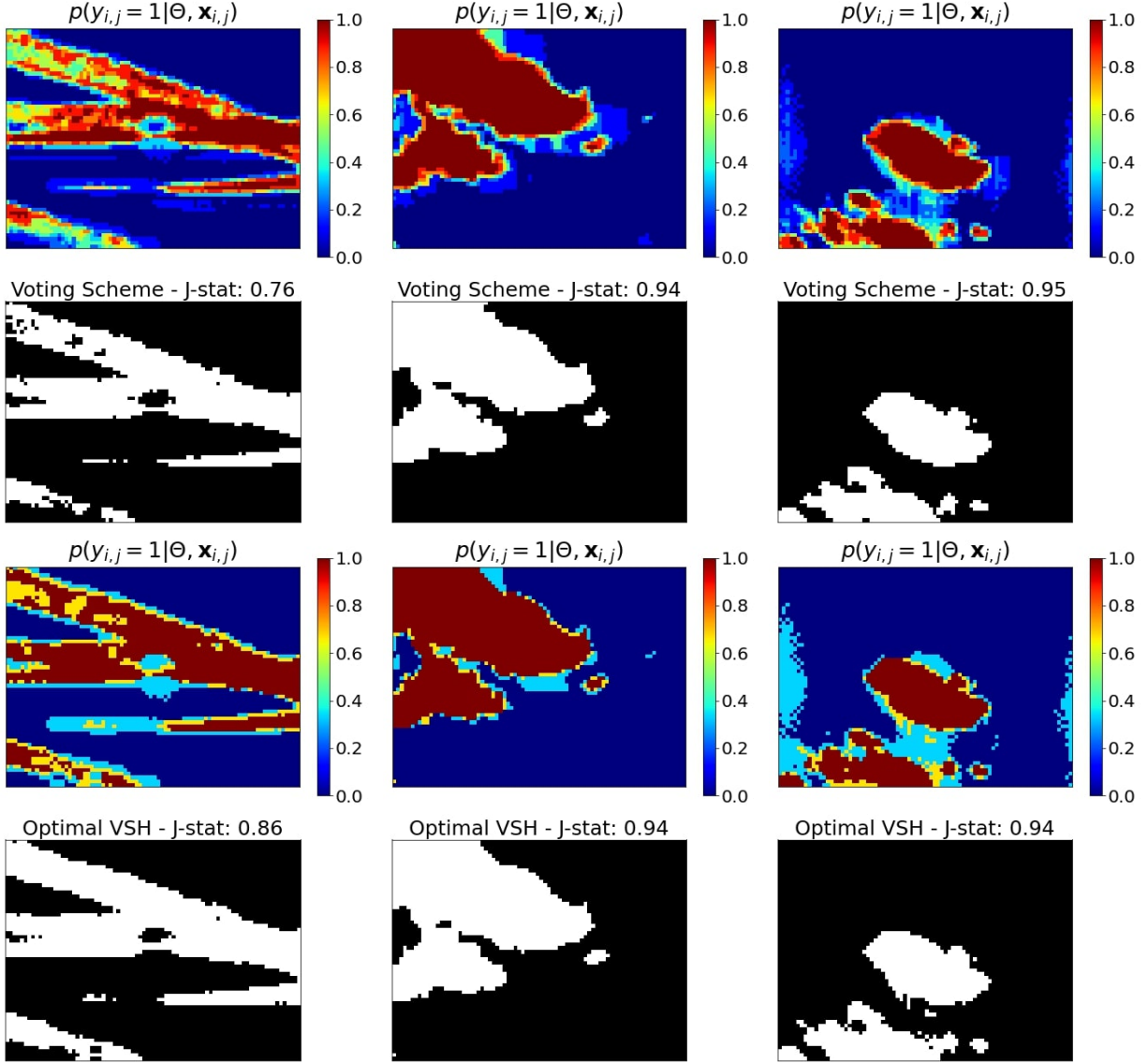


Figure 9: The three different test images are shown in the columns. The images in the first and second row show the results of the voting scheme. The images in the first row display the probability of a pixel belonging to a cloud. The images in the second row show the segmentation performed by the voting scheme. The images in the third and fourth row show the probability of a pixel belonging to a cloud and the segmentation of the optimal voting scheme (VSH). The j-stat is the score that the method achieved in the test image.

Preprocessing the IR images using both the window and atmospheric models leads to an improvement of overall performance of the segmentation algorithms. Simplification of the covariance matrix reduces the computing time, but the j-statistic achieved is lower than that of the models using the full covariance matrix. Adding the features of neighboring pixels to the feature vectors yields an increase in segmentation performances in some cases. The discriminate models formulated in the primal result in feasible segmentation models for real-time application. MRF models remove possible outliers using cliques from neighboring pixels. This increases the overall performance of the generative models when trained with unsupervised and supervised algorithms. The optimal voting scheme achieved the best j-statistic. However, the implementation computing time might be slow for real-time applications when not run in parallel.

Further investigation may study the performances of sparse Kernel methods for clouds segmentation. Another interesting emphasis would be the implementation of cloud segmentation when there are multiple layers of clouds. The clouds in each layer may be segmented in different classes. An algorithm can be trained to detect multiple layers of clouds when

clouds have different heights or directions. In this way, the extraction of features may be independently performed in each one of the cloud layers. The algorithm for the segmentation of multiple layers of clouds will reduce the noise in feature extraction. This algorithm may be implemented to increase the performance of ground-based very short-term GSI forecasting. The algorithm also may be used in both short-term and medium-term GSI forecasting when it is applied to satellite IR images instead.

8 Acknowledgments

This work has been supported by NSF EPSCoR grant number OIA-1757207 and the King Felipe VI endowed Chair. Authors would like to thank the UNM Center for Advanced Research Computing, supported in part by the National Science Foundation, for providing the high performance computing and large-scale storage resources used in this work.

References

- [1] William Zappa, Martin Junginger, and Machteld van den Broek. Is a 100% renewable european power system feasible by 2050? *Applied Energy*, 233-234:1027 – 1050, 2019.
- [2] D. Mateos, M. Antón, A. Valenzuela, A. Cazorla, F.J. Olmo, and L. Alados-Arboledas. Efficiency of clouds on shortwave radiation using experimental data. *Applied Energy*, 113:1216 – 1219, 2014.
- [3] Xiaoyang Chen, Yang Du, Enggee Lim, Huiqing Wen, Ke Yan, and James Kirtley. Power ramp-rates of utility-scale pv systems under passing clouds: Module-level emulation with cloud shadow modeling. *Applied Energy*, 268:114980, 2020.
- [4] Kari Lappalainen and Seppo Valkealahti. Output power variation of different pv array configurations during irradiance transitions caused by moving clouds. *Applied Energy*, 190:902 – 910, 2017.
- [5] Francesco Crespi, Andrea Toscani, Paolo Zani, David Sánchez, and Giampaolo Manzolini. Effect of passing clouds on the dynamic performance of a csp tower receiver with molten salt heat storage. *Applied Energy*, 229:224 – 235, 2018.
- [6] Claudia Furlan, Amauri Pereira de Oliveira, Jacyra Soares, Georgia Codato, and João Francisco Escobedo. The role of clouds in improving the regression model for hourly values of diffuse solar radiation. *Applied Energy*, 92:240 – 254, 2012.
- [7] Michael John De Smith, Michael F Goodchild, and Paul Longley. *Geospatial analysis: a comprehensive guide to principles, techniques and software tools*. Troubador publishing ltd, 2007.
- [8] William J Randel, Fei Wu, and Dian J Gaffen. Interannual variability of the tropical tropopause derived from radiosonde data and ncep reanalyses. *Journal of Geophysical Research: Atmospheres*, 105(D12):15509–15523, 2000.
- [9] Robert A Houze Jr. *Cloud dynamics*. Academic press, 2014.
- [10] C. Deng, Z. Li, W. Wang, S. Wang, L. Tang, and A. C. Bovik. Cloud detection in satellite images based on natural scene statistics and gabor features. *IEEE Geoscience and Remote Sensing Letters*, 16(4):608–612, April 2019.
- [11] Richard Perez, Sergey Kivalov, James Schlemmer, Karl Hemker, David Renné, and Thomas E. Hoff. Validation of short and medium term operational solar radiation forecasts in the us. *Solar Energy*, 84(12):2161 – 2172, 2010.
- [12] M. Bouzerdoun, A. Mellit, and A. Massi Pavan. A hybrid model (sarima–svm) for short-term power forecasting of a small-scale grid-connected photovoltaic plant. *Solar Energy*, 98:226 – 235, 2013.
- [13] A. Mellit, A. Massi Pavan, and V. Lughi. Short-term forecasting of power production in a large-scale photovoltaic plant. *Solar Energy*, 105:401 – 413, 2014.
- [14] S. Salcedo-Sanz, C. Casanova-Mateo, A. Pastor-Sánchez, and M. Sánchez-Girón. Daily global solar radiation prediction based on a hybrid coral reefs optimization – extreme learning machine approach. *Solar Energy*, 105:91 – 98, 2014.
- [15] Philippe Lauret, Cyril Voyant, Ted Soubdhan, Mathieu David, and Philippe Poggi. A benchmarking of machine learning techniques for solar radiation forecasting in an insular context. *Solar Energy*, 112:446 – 457, 2015.
- [16] O. García-Hinde, G. Terrén-Serrano, M.Á. Hombrados-Herrera, V. Gómez-Verdejo, S. Jiménez-Fernández, C. Casanova-Mateo, J. Sanz-Justo, M. Martínez-Ramón, and S. Salcedo-Sanz. Evaluation of dimensionality reduction methods applied to numerical weather models for solar radiation forecasting. *Engineering Applications of Artificial Intelligence*, 69:157 – 167, 2018.

- [17] Patrick Mathiesen, Craig Collier, and Jan Kleissl. A high-resolution, cloud-assimilating numerical weather prediction model for solar irradiance forecasting. *Solar Energy*, 92:47 – 61, 2013.
- [18] Hou Jiang, Ning Lu, Guanghui Huang, Ling Yao, Jun Qin, and Hengzi Liu. Spatial scale effects on retrieval accuracy of surface solar radiation using satellite data. *Applied Energy*, 270:115178, 2020.
- [19] Abhnil A. Prasad, Robert A. Taylor, and Merlinde Kay. Assessment of direct normal irradiance and cloud connections using satellite data over australia. *Applied Energy*, 143:301 – 311, 2015.
- [20] Hsu-Yung Cheng. Cloud tracking using clusters of feature points for accurate solar irradiance nowcasting. *Renewable Energy*, 104:281 – 289, 2017.
- [21] Jui-Sheng Chou and Ngoc-Son Truong. Cloud forecasting system for monitoring and alerting of energy use by home appliances. *Applied Energy*, 249:166 – 177, 2019.
- [22] Guillermo Terrén-Serrano and Manel Martínez-Ramón. Multi-layer wind velocity field visualization in infrared images of clouds, 2020.
- [23] Shin ichi Inage. Development of an advection model for solar forecasting based on ground data first report: Development and verification of a fundamental model. *Solar Energy*, 153:414 – 434, 2017.
- [24] Weicong Kong, Youwei Jia, Zhao Yang Dong, Ke Meng, and Songjian Chai. Hybrid approaches based on deep whole-sky-image learning to photovoltaic generation forecasting. *Applied Energy*, 280:115875, 2020.
- [25] H.-Y. Cheng and C.-L. Lin. Cloud detection in all-sky images via multi-scale neighborhood features and multiple supervised learning techniques. *Atmospheric Measurement Techniques*, 10(1):199–208, 2017.
- [26] Chia-Lin Fu and Hsu-Yung Cheng. Predicting solar irradiance with all-sky image features via regression. *Solar Energy*, 97:537 – 550, 2013.
- [27] Chaojun Shi, Yatong Zhou, Bo Qiu, Jingfei He, Mu Ding, and Shiya Wei. Diurnal and nocturnal cloud segmentation of all-sky imager (asi) images using enhancement fully convolutional networks. *Atmospheric Measurement Techniques*, 12:4713–4724, 09 2019.
- [28] Alireza Taravat, F. Del Frate, Cristina Cornaro, and Stefania Vergari. Neural networks and support vector machine algorithms for automatic cloud classification of whole-sky ground-based images. *IEEE Geoscience and Remote Sensing Letters*, 12, 02 2015.
- [29] Chi Wai Chow, Bryan Urquhart, Matthew Lave, Anthony Dominguez, Jan Kleissl, Janet Shields, and Byron Washom. Intra-hour forecasting with a total sky imager at the uc san diego solar energy testbed. *Solar Energy*, 85(11):2881 – 2893, 2011.
- [30] S. Dev, Y. H. Lee, and S. Winkler. Color-based segmentation of sky/cloud images from ground-based cameras. *IEEE Journal of Selected Topics in Applied Earth Observations and Remote Sensing*, 10(1):231–242, Jan 2017.
- [31] H. Li, F. Wang, H. Ren, H. Sun, C. Liu, B. Wang, J. Lu, Z. Zhen, and X. Liu. Cloud identification model for sky images based on otsu. In *International Conference on Renewable Power Generation (RPG 2015)*, pages 1–5, Oct 2015.
- [32] L. Ye, Z. Cao, Y. Xiao, and Z. Yang. Supervised fine-grained cloud detection and recognition in whole-sky images. *IEEE Transactions on Geoscience and Remote Sensing*, 57(10):7972–7985, Oct 2019.
- [33] Dazhi Yang, Jan Kleissl, Christian A Gueymard, Hugo TC Pedro, and Carlos FM Coimbra. History and trends in solar irradiance and pv power forecasting: A preliminary assessment and review using text mining. *Solar Energy*, 168:60–101, 2018.
- [34] M.I. Gohari, B. Urquhart, H. Yang, B. Kurtz, D. Nguyen, C.W. Chow, M. Ghonima, and J. Kleissl. Comparison of solar power output forecasting performance of the total sky imager and the university of california, san diego sky imager. *Energy Procedia*, 49:2340 – 2350, 2014. Proceedings of the SolarPACES 2013 International Conference.
- [35] Ricardo Marquez and Carlos F.M. Coimbra. Intra-hour dni forecasting based on cloud tracking image analysis. *Solar Energy*, 91:327 – 336, 2013.
- [36] Andrea Mammoli, Guillermo Terren-Serrano, Anthony Menicucci, Thomas P Caudell, and Manel Martínez-Ramón. An experimental method to merge far-field images from multiple longwave infrared sensors for short-term solar forecasting. *Solar Energy*, 187:254–260, 2019.
- [37] H. Escrig, Francisco Batlles, Joaquín Alonso-Montesinos, F.M. Baena, Juan Bosch, I. Salbidegoitia, and Juan Burgaleta. Cloud detection, classification and motion estimation using geostationary satellite imagery for cloud cover forecast. *Energy*, 55, 06 2013.
- [38] Joseph A. Shaw, Paul W. Nugent, Nathan J. Pust, Brentha Thurairajah, and Kohei Mizutani. Radiometric cloud imaging with an uncooled microbolometer thermal infrared camera. *Opt. Express*, 13(15):5807–5817, Jul 2005.

- [39] Joseph A Shaw and Paul W Nugent. Physics principles in radiometric infrared imaging of clouds in the atmosphere. *European Journal of Physics*, 34(6):S111–S121, oct 2013.
- [40] B. Thurairajah and J. A. Shaw. Cloud statistics measured with the infrared cloud imager. *IEEE Transactions on Geoscience and Remote Sensing*, 43(9):2000–2007, Sep. 2005.
- [41] Paul W. Nugent, Joseph A. Shaw, and Sabino Piazzolla. Infrared cloud imaging in support of earth-space optical communication. *Opt. Express*, 17(10):7862–7872, May 2009.
- [42] Nathan J. Pust Paul W. Nugent, Joseph A. Shaw. Correcting for focal-plane-array temperature dependence in microbolometer infrared cameras lacking thermal stabilization. *Optical Engineering*, 52(6):1–8, 2013.
- [43] X. Hu, Y. Wang, and J. Shan. Automatic recognition of cloud images by using visual saliency features. *IEEE Geoscience and Remote Sensing Letters*, 12(8):1760–1764, Aug 2015.
- [44] Cunzhao Shi, Yu Wang, Chunheng Wang, and Baihua Xiao. Ground-based cloud detection using graph model built upon superpixels. *IEEE Geoscience and Remote Sensing Letters*, 14(5):719–723, 2017.
- [45] Ernst Ising. Beitrag zur Theorie des Ferromagnetismus. *Zeitschrift fur Physik*, 31(1):253–258, February 1925.
- [46] Lars Onsager. Crystal statistics. i. a two-dimensional model with an order-disorder transition. *Phys. Rev.*, 65:117–149, Feb 1944.
- [47] Julian Besag. On the statistical analysis of dirty pictures. *Journal of the Royal Statistical Society B*, 48(3):48–259, 1986.
- [48] C. Papin, P. Bouthemy, and G. Rochard. Unsupervised segmentation of low clouds from infrared meteosat images based on a contextual spatio-temporal labeling approach. *IEEE Transactions on Geoscience and Remote Sensing*, 40(1):104–114, Jan 2002.
- [49] Qingyong Li, Weitao Lyu, Jun Yang, and James Wang. Thin cloud detection of all-sky images using markov random fields. *IEEE Geoscience and Remote Sensing Letters*, 9:417–421, 05 2012.
- [50] S. Liu, L. Zhang, Z. Zhang, C. Wang, and B. Xiao. Automatic cloud detection for all-sky images using superpixel segmentation. *IEEE Geoscience and Remote Sensing Letters*, 12(2):354–358, Feb 2015.
- [51] Wen Zhuo, Zhiguo Cao, and Yang Xiao. Cloud Classification of Ground-Based Images Using Texture–Structure Features. *Journal of Atmospheric and Oceanic Technology*, 31(1):79–92, 01 2014.
- [52] Johannes Dröner, Nikolaus Korfhage, Sebastian Egli, Markus Mühlhling, Boris Thies, Jörg Bendix, Bernd Freisleben, and Bernhard Seeger. Fast cloud segmentation using convolutional neural networks. *Remote Sensing*, 10:1782, 11 2018.
- [53] Jinglin Zhang, Liu Pu, Feng Zhang, and Qianqian Song. Cloudnet: Ground-based cloud classification with deep convolutional neural network. *Geophysical Research Letters*, 08 2018.
- [54] Guillermo Terrén-Serrano and Manel Martínez-Ramón. Data acquisition and image processing for solar irradiance forecast, 2020.
- [55] S.L. Hess. *Introduction to Theoretical Meteorology*. Holt-Dryden book. Holt, 1959.
- [56] Peter H Stone and John H Carlson. Atmospheric lapse rate regimes and their parameterization. *Journal of the Atmospheric Sciences*, 36(3):415–423, 1979.
- [57] JR Hummel and WR Kuhn. Comparison of radiative-convective models with constant and pressure-dependent lapse rates. *Tellus*, 33(3):254–261, 1981.
- [58] L. L. Pan and L. A. Munchak. Relationship of cloud top to the tropopause and jet structure from calipso data. *Journal of Geophysical Research: Atmospheres*, 116(D12), 2011.
- [59] Simon Baker, Ralph Gross, Takahiro Ishikawa, and Iain Matthews. Lucas-kanade 20 years on: A unifying framework: Part 2. *International Journal of Computer Vision*, 56:221–255, 2003.
- [60] Alex J. Smola and Bernhard Schölkopf. Sparse greedy matrix approximation for machine learning. In *Proc. 17th International Conf. on Machine Learning*, pages 911–918. Morgan Kaufmann, San Francisco, CA, 2000.
- [61] Trevor Hastie, Robert Tibshirani, and Jerome Friedman. *The Elements of Statistical Learning*. Springer Series in Statistics. Springer New York Inc., 2001.
- [62] Kevin P Murphy. *Machine learning: a probabilistic perspective*. MIT press, 2012.
- [63] E. Forgy. Cluster analysis of multivariate data: Efficiency versus interpretability of classification. *Biometrics*, 21(3):768–769, 1965.
- [64] Stan Z. Li. *Markov Random Field Modeling in Image Analysis*. Springer-Verlag, Berlin, Heidelberg, 2001.

- [65] J. M. Hammersley and P. Clifford. Markov fields on finite graphs and lattices. Unpublished, 1971.
- [66] Zoltan Kato and Ting-Chuen Pong. A markov random field image segmentation model using combined color and texture features. In Władysław Skarbek, editor, *Computer Analysis of Images and Patterns*, pages 547–554. Springer Berlin Heidelberg, 2001.
- [67] S. Kirkpatrick, C. D. Gelatt, and M. P. Vecchi. Optimization by simulated annealing. *Science*, 220(4598):671–680, 1983.
- [68] Angel Navia-Vazquez, Fernando Pérez-Cruz, Antonio Artes-Rodríguez, and Aníbal R Figueiras-Vidal. Weighted least squares training of support vector classifiers leading to compact and adaptive schemes. *IEEE Transactions on Neural Networks*, 12(5):1047–1059, 2001.
- [69] Rong-En Fan, Kai-Wei Chang, Cho-Jui Hsieh, Xiang-Rui Wang, and Chih-Jen Lin. Liblinear: A library for large linear classification. *J. Mach. Learn. Res.*, 9:1871–1874, June 2008.
- [70] Chih-Wei Hsu, Chih-Chung Chang, and Chih-Jen Lin. A practical guide to support vector classification, 2010.
- [71] Christopher Williams and Carl Edward Rasmussen. *Gaussian processes for machine learning*, volume 2. MIT press Cambridge, MA, 2006.
- [72] Tommi Jaakkola and Michael Jordan. A variational approach to bayesian logistic regression models and their extensions, 1997.
- [73] W. J. Youden. Index for rating diagnostic tests. *Cancer*, 3(1):32–35, 1950.
- [74] Tom Fawcett. An introduction to roc analysis. *Pattern Recognition Letters*, 27(8):861–874, June 2006.
- [75] X. Blasco, J.M. Herrero, J. Sanchis, and M. Martínez. A new graphical visualization of n-dimensional pareto front for decision-making in multiobjective optimization. *Information Sciences*, 178(20):3908 – 3924, 2008. Special Issue on Industrial Applications of Neural Networks.